Solid Earth, 13, 1803–1821, 2022
https://doi.org/10.5194/se-13-1803-2022

Solid Earth

Epidote dissolution–precipitation during viscous granular flow: a micro-chemical and isotope study

Veronica Peverelli[1], **Alfons Berger**[1], **Martin Wille**[1], **Thomas Pettke**[1], **Pierre Lanari**[1], **Igor Maria Villa**[1,2], **and Marco Herwegh**[1]

[1]Department of Geological Sciences, University of Bern, 3012 Bern, Switzerland
[2]Dipartimento di Scienze dell'Ambiente e della Terra, University of Milano-Bicocca, 20126 Milan, Italy

Correspondence: Veronica Peverelli (veronica.peverelli@geo.unibe.ch)

Received: 7 May 2022 – Discussion started: 20 May 2022
Revised: 19 August 2022 – Accepted: 24 October 2022 – Published: 22 November 2022

Abstract. Deformation of polymineralic aggregates can be accommodated by viscous granular flow, a process mediated by the interplay among intracrystalline plasticity and dissolution–precipitation, each active in specific minerals under given P–T conditions. Some rock-forming minerals like quartz and feldspars have been intensively studied in terms of deformation processes. Instead, the deformation behavior of epidote and its role during viscous granular flow is not well investigated, although this mineral is ubiquitous in granitic rocks deforming under greenschist-facies conditions. In this contribution, we provide microstructural and geochemical evidence for the occurrence of dissolution–precipitation of epidote during deformation of an epidote–quartz vein. The main part of the vein is deformed, producing a fold, which is visible due to relicts of primary-growth layering inside the vein. The deformation mechanisms active during deformation include dynamic recrystallization of quartz by subgrain rotation recrystallization, producing grain size reduction in the primary vein quartz. Recrystallization occurs contemporaneously with dissolution and (re)precipitation of epidote and quartz grain boundary sliding, leading to a combined process described as viscous granular flow. The combination of grain boundary sliding and dissolution locally and repeatedly produces creep cavities. These represent not only loci for nucleation of new epidote grains at the expense of dissolved ones, but they also allow fluid-mediated transport of elements. The same trace element patterns between old epidote relicts and newly formed grains, with much narrower variability in the latter, indicate a process of chemical homogenization. The nature of the fluid that mediates deformation is investigated using Pb–Sr isotope data of epidote, which suggest that deformation is assisted by internally recycled fluids with the addition of a syn-kinematic external fluid component.

---

1 Introduction

Deformation microstructures preserved in rocks are the result of the interplay of multiple microscale deformational processes, which may be identified and appreciated through careful petrographic studies (e.g., Passchier, 2005). These processes – which may be coupled to metamorphic reactions and diffusion (e.g., Pearce et al., 2013; Wintsch and Yeh, 2013; Bukovská et al., 2016; Giuntoli et al., 2018; Lanari and Duesterhoeft, 2019) – are the response of the grains to varying physico-chemical conditions in order to minimize the system's internal energy (e.g., Evans et al., 2001; Herwegh and Berger, 2004; Passchier, 2005; Karato, 2008; Herwegh et al., 2011; Hobbs et al., 2010). Microstructures of monomineralic aggregates are determined by the deformation behavior of the constituent mineral and by the physical conditions (e.g., temperature, stress, availability of fluids) existing during deformation. For example, Stipp et al. (2002) showed that the microstructures resulting from dynamic recrystallization of quartz can be linked to different recrystallization mechanisms active at increasing temperatures and strain rates. However, this type of interpretation is more complicated when dealing with polymineralic aggregates, where the modal amounts and specific deformation mechanisms of each mineral have an effect on the deformation behavior of the bulk system (e.g., Handy, 1990, 1994; Olgaard, 1990;

Stünitz and Fitz Gerald, 1993; Kruse and Stünitz, 1999; Tullis, 2002; Herwegh and Berger, 2004; Passchier, 2005; Herwegh et al., 2011; Wehrens et al., 2017). In this context, mass transfer processes like dissolution–precipitation play a fundamental role in that they enable the redistribution of material within the deforming system (e.g., Paterson, 1995; Herwegh and Jenni, 2001; Konrad-Schmolke et al., 2018). The essential requisite for dissolution–precipitation processes to occur is the presence of a fluid phase (e.g., Putnis, 2009; Putnis and Austrheim, 2010; Putnis and John, 2010). In the presence of a fluid, dissolved material may precipitate inside intergranular voids during deformation. In this scenario, the process of dissolution–precipitation in combination with the presence of a second phase keeps the grain sizes of the deforming aggregate small in a process called viscous granular flow (Olgaard, 1990; Fitz Gerald and Stünitz, 1993; Stünitz and Fitz Gerald, 1993; Paterson, 1995; Herwegh and Berger, 2004; Herwegh et al., 2011). Viscous granular flow is a mechanism in which grains slide relative to one another: this process requires grain size reduction and plastic material transfer and/or dissolution–precipitation processes (or solution transfer) at the scale of the deforming polymineralic aggregate in order to facilitate grain boundary sliding (Stünitz and Fitz Gerald, 1993; Paterson, 1995). Grain boundary sliding promotes the formation of creep cavities, hence allowing the nucleation of second-phase minerals (e.g., Herwegh and Jenni, 2001; Fusseis et al., 2009; Gilgannon et al., 2021). Fluids play a crucial role in deformation processes, but it is often unclear whether the fluids are newly added to the system during deformation (i.e., of external origin) or whether they are recycled (e.g., via dissolution of hydrous minerals). Hence, the interplay of recycled and newly added fluids, mass-transfer processes, and deformation mechanisms to produce complex microstructures remains to be fully appreciated.

In this contribution, via combined microstructural observations, geochemical data, and Pb–Sr isotope geochemistry, we investigate the deformational processes affecting epidote (i.e., $Ca_2Al_2(Al,Fe^{3+})Si_3O_{12}(OH)$) in a folded epidote–quartz hydrothermal vein deformed by shearing. The nature of the fluid assisting folding is investigated using Pb and Sr isotope data. Epidote group minerals are widespread rock-forming, hydrothermal, and alteration minerals in granitic rocks (e.g., Bird and Spieler, 2004; Enami et al., 2004; Franz and Liebscher, 2004; Grapes and Hoskin, 2004; Schmidt and Poli, 2004; Morad et al., 2010; Hentschel et al., 2020), and they allegedly behave similarly during deformation. Therefore, the occurrence of epidote dissolution–precipitation and its control on the deformation mechanisms of other rock-forming minerals has important implications for the structural evolution of granitoids, among other epidote-bearing rocks, during orogenic phases.

2 Geological setting

The Grimsel Pass area (Fig. 1; central Swiss Alps, Switzerland) is in the southern part of the Aar Massif, one of the external crystalline massifs of the Alps (e.g., Schneeberger et al., 2019; Berger et al., 2017a). The Aar Massif consists of a Paleozoic polymetamorphic basement and Permian intrusives, including the post-Variscan Central Aar Granite. This granitoid was emplaced 299 ± 2 Ma (Schaltegger and Corfu, 1992; Ruiz et al., 2022) and bears clear evidence of Alpine deformation (e.g., Choukroune and Gapais, 1983; Bambauer et al., 2009; and references therein). This Alpine deformation is expressed by a large number of ductile shear zones, and in the southern Aar Massif it can be subdivided into two major phases: (1) a reverse faulting phase with green biotite stable in the shear zones at >400 °C (ca. 22–17 Ma; Challandes et al., 2008; Rolland et al., 2009; Wehrens et al., 2017) and (2) a strike-slip phase at lower temperatures with chlorite progressively replacing biotite in the shear zones (from ca. 14 Ma onwards; Rolland et al., 2009; Wehrens et al., 2017; Herwegh et al., 2020). The Alpine metamorphic overprint reached greenschist-facies conditions in the area, with maximum temperatures and pressures of 450 ± 30 °C and 6 ± 1 kbar, respectively (Challandes et al., 2008; Goncalves et al., 2012; Villa and Hanchar, 2013). Hydrothermal activity upon exhumation in Alpine times is recorded in the area primarily by the Grimsel Breccia Fault hydrothermal system (e.g., Hofmann et al., 2004; Belgrano et al., 2016; Diamond et al., 2018; Egli et al., 2018). U–Pb geochronology of hydrothermal epidote in veins returned Miocene ages (19.2 ± 4.3 Ma and 16.9 ± 3.7 Ma; Peverelli et al., 2021) related to fluid circulation occurring during the Alpine orogenic phases, already described also on the basis of cleft mineralization (e.g., Mullis et al., 1994; Janots et al., 2012; Berger et al., 2013, 2022; Rossi and Rolland, 2014; Bergemann et al., 2017b; Ricchi et al., 2019). In addition, Permian ages (279 ± 29, 291 ± 50, and 275 ± 18 Ma) returned by other epidote veins revealed pre-orogenic fluid circulation in the Grimsel Pass area (Peverelli et al., 2022).

3 Field relations and sample description

The investigated sample is called Grimsel-1, and it is an epidote–quartz (± biotite) vein that was collected in the Grimsel Pass area inside the Grimsel test site (GTS), which is the underground rock laboratory of Nagra (Figs. 1 and 2a). The GTS is a ca. 500 m long tunnel designed to study rock properties and fluid circulation in the area (see Schneeberger et al., 2019). In the GTS, the anastomosing pattern of shear zones (e.g., Wehrens et al., 2017) is well exposed on the tunnel walls. The studied epidote vein is associated with a WSW–ENE-striking and a steeply NNW-dipping shear zone of Alpine age hosted by the Central Aar Granite (Fig. 2b). The shear zone is ca. 10 cm wide, whereas the epidote vein

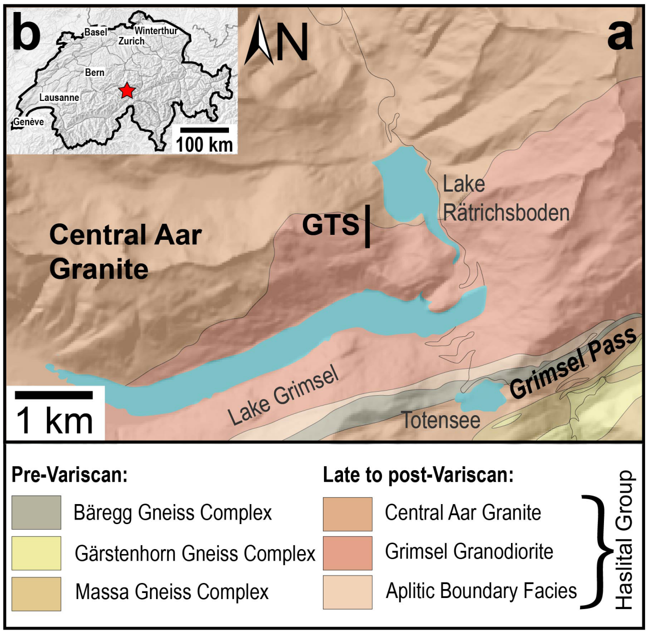

Figure 1. **(a)** Geological map of the Grimsel Pass area (redrawn from Wehrens et al., 2016). **(b)** Geographic location of the Grimsel Pass area (red star) in Switzerland (modified from https://www.map.geo.admin.ch; last access: 11 November 2022). The digital elevation model in panel **(a)** is from https://www.map.geo.admin.ch; last access: 11 November 2022.

(Grimsel-1 in Fig. 2b) reaches up to a couple of centimeters in width and ca. 50 cm in length on the tunnel wall.

The Central Aar Granite is the vein's host, and it displays a gradation from slightly to highly deformed; this is expressed by increasingly intense foliation and decreasing grain size moving towards the shear zone (Fig. 2b). In the thin section (Fig. 3), the host rock mostly preserves its magmatic texture, and it is made of ca. 55 vol. % of altered feldspar and 35 vol. % quartz. Feldspar grains are sometimes fractured. Relict plagioclase and K-feldspar grains can be recognized by the different type and extent of alteration. Plagioclase (ca. 20 vol. %) is highly altered into epidote and white mica, to a larger extent in the cores than in the rims of the grains. Exsolution lamellae are preserved in K-feldspar grains (ca. 35 vol. %), which are moderately altered into sericite. Green biotite, epidote, and minor chlorite define a weak foliation and make up ca. 10 vol. %, with a few accessory titanite grains completing the host rock's mineral assemblage. A detailed description of the host rock is outside the scope of this contribution, and it is presented in Schneeberger et al. (2009).

The sharp boundary between host and vein is marked by a change in modal abundances in epidote and quartz. The object of the present investigation is Grimsel-1 epidote–quartz vein (Fig. 3; already used in Peverelli et al., 2021, 2022). This vein is subdivided into three layers: (1) layer with coarse-grained epidote (Fig. 4d), quartz, and minor green biotite; (2) heavily deformed and finer-grained epidote–quartz

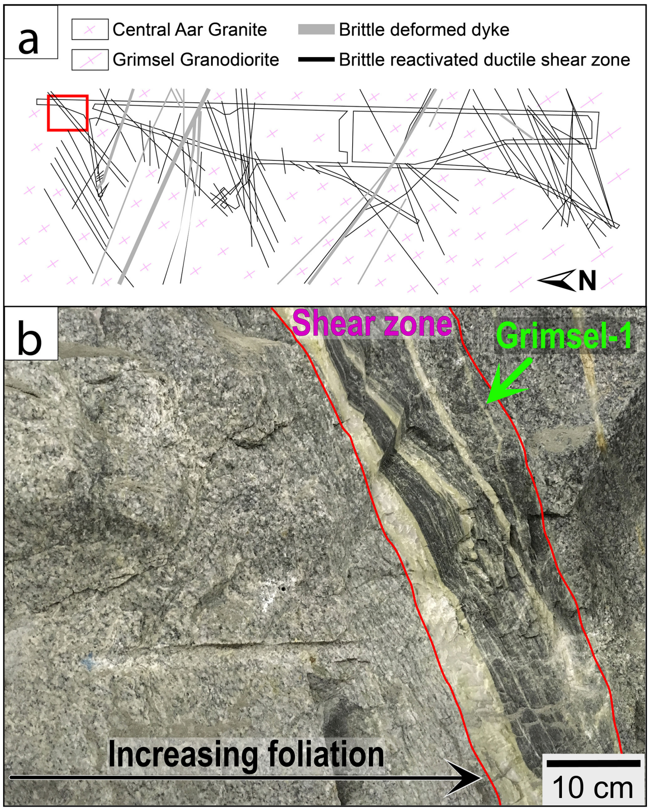

Figure 2. **(a)** Geological map of the Grimsel test site (GTS) of Nagra with the location of **(b)** shown in the red rectangle (redrawn from Schneeberger et al., 2019). **(b)** Field photograph of the location of the studied epidote–quartz vein (Grimsel-1) and the steeply NNW-dipping Alpine shear zone with which it is associated; both are in the Central Aar Granite, which shows increasing foliation towards the shear zone (modified from Peverelli et al., 2022).

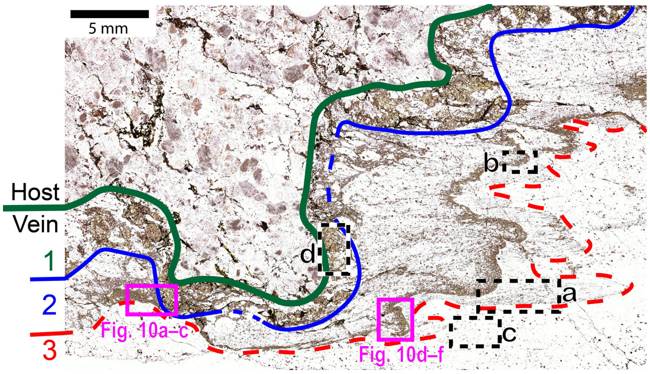

Figure 3. Transmitted-light microscope scan of the studied epidote–quartz (± biotite) vein and the host Central Aar Granite. The numbers 1–3 refer to the vein layers described in Sect. 3. Dashed rectangles a–d indicate the locations of the microstructural domains shown in Fig. 4a–d. The pink rectangles indicate the locations of Fig. 10a–c (rotated 90° clockwise) and Fig. 10d–f (rotated 180°). Plane-polarized light.

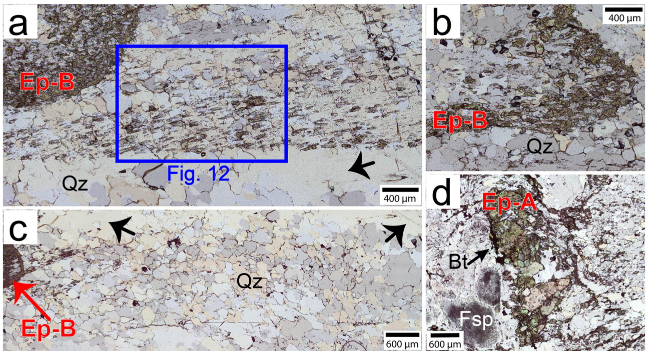

Figure 4. Transmitted-light scans of the microstructural domains described in Sect. 5.1. Microstructures in **(a–c)** are used for microstructural analysis (Fig. 7, Sect. 5.1.2). The blue rectangle in **(a)** indicates the location of the cathodoluminescence image of Fig. 12. Bt: biotite; Ep-A: Epidote-A; Ep-B: Epidote-B; Fsp: feldspar; Qz: quartz. Plane-polarized light. The anomalous birefringence is due to the thickness of the section (ca. 60 µm).

layer (Fig. 4a–b); and (3) nearly pure quartz layer (Fig. 4c). Grain sizes and mineral proportions in each layer are given in Table 1. Layers 2–3 are strongly deformed and folded, as indicated by the spatial distribution of epidote and quartz (Figs. 3 and 4a–b). Layer 1, on the other hand, is less affected by this folding process (Figs. 3 and 4d). The modal abundance of green biotite varies greatly among the three layers, with a sharp decrease from layer 1 to layer 2, and layer 3 being devoid of biotite (Table 1). The transition from layer 2 to layer 3 is marked by a change in the epidote/quartz ratio. This is up to ca. 40/60 in layer 2, whereas layer 3 is characterized by the near absence of epidote. Peverelli et al. (2021; see their Fig. 6b) performed U–Pb dating by laser ablation inductively coupled plasma mass spectrometry (LA-ICP-MS) of epidote grains in layer 1, obtaining a Tera–Wasserburg age of 19.2 ± 4.3 Ma. The Tera–Wasserburg regression revealed a single epidote generation at the current analytical precision (i.e., mean square of weighted deviates, MSWD, of 0.79), and the age is interpreted as the timing of epidote crystallization upon vein opening (Peverelli et al., 2021). The focus of this paper is the deformation mechanisms in layers 2–3.

4 Methods

Analyses were performed at the Institute of Geological Sciences of the University of Bern (Switzerland). The petrographic characterization of the studied sample was done in a ca. 60 µm thick section on a Zeiss Axioplan petrographic microscope. For backscattered electron (BSE), forescattered electron (FSE), and cathodoluminescence (CL) images, and for electron backscatter diffraction (EBSD), a Zeiss EVO50 scanning electron microscope (SEM) was used with a beam current of ca. 1 nA and accelerating voltage of 20 kV.

4.1 Grain size analysis

Microstructural analysis was performed combining transmission light and scanning electron microscopy to determine average grain sizes of epidote and quartz, as well as their volume fractions in selected microstructural domains. Grain size analysis was carried out in ImageJ (IJ 1.46r; Ferreira and Wayne, 2012) using sketches of the microstructures drawn on transmitted-light, BSE, and FSE images. In domains where the microstructure is not suitable for an automated grain size analysis by ImageJ (Figs. 4b, 6, and 7c), epidote and quartz areas were directly measured on a transmitted-light microscope, approximated as ellipses. Epidote grains that are isolated among quartz grains are defined by the presence of epidote–quartz boundaries. Grain boundaries among or between epidote grains are defined as any irregular discontinuity between grains that is confirmed by different extinction angles at the optic microscope (i.e., misorientations of $\geq 2.5°$). Quartz grains are identified by the presence of visible grain boundaries in BSE images and confirmed by observations of differences in extinction angles at the optic microscope. The equivalent diameter of each grain (D) is calculated from the grain areas (A) as $D = 2 \times \sqrt{A/\pi}$.

4.2 Chemical maps

X-ray compositional maps in wavelength dispersive mode of Si, Fe, Al, Ca, Mn, and Sr were obtained by an electron probe micro-analyzer (EPMA) on a JEOL-8200 microprobe. Accelerating voltage was 15 keV, specimen current was 100 nA, the step size was 4 µm, and dwell times were 190 ms (map of layers 1–3; Fig. 10a–c) and 180 ms (map of layer 2; Fig. 10d–f). For calibration of the X-ray maps, spot analyses were acquired with a specimen current of 10 nA and calibrated using the following standards: wollastonite (SiO_2), olivine (MgO), anorthite (CaO, Al_2O_3), magnetite (FeO), pyrolusite (MnO), tugtupite (Cl), rutile (TiO_2), and celestite (SrO). The processing of the X-ray compositional maps, including map calibration, was done by using XMapTools (Lanari et al., 2014, 2019). Minerals were identified based on the concentrations of specific elements (i.e., Ca, Fe, and Al for epidote; Si for quartz; K for micas) and classified. Maps of the structural formula of epidote were calculated on a 12.5 oxygen basis.

4.3 Trace elements

For trace element measurements, a RESOlutionSE 193 nm excimer laser system (Applied Spectra, USA) equipped with an S-155 large-volume, constant-geometry chamber (Laurin Technic, Australia) coupled with an Agilent 7900 ICP-QMS was employed. During ablation, a He atmosphere was used, and Ar was admixed to the carrier gas before reaching the plasma of the ICP-MS. NIST SRM612 was used for optimization of the analytical conditions, ensuring that the ThO production rate was <0.2 % and the Th/U sensitivity

Table 1. Main characteristics of the vein layers. Ep: epidote; Qz: quartz; vol.: volume.

Layer	Minerals other than Ep + Qz	Ep [vol. %]	Ep grain size	Qz grain size	Qz relicts
1	Green biotite (ca. 5 vol. %)	ca. 70	0.025–1.6 mm	80–400 µm	0.6–1.2 mm
2	Green biotite (ca. 1 vol. %)	ca. 5–40	5–90 µm	20–170 µm	1.4–2.5 mm
3	–	<1	5–200 µm	30–400 µm	0.6–2 cm

ratio >97 %. On-sample fluence was 5 J cm^{-2}, with a repetition rate of 5 Hz. The size of the analysis spots ranged between 20–30 µm, and BSE images were used to plan the analyses to avoid locating any spots across zones with heterogeneous composition (e.g., chemical zoning) or on inclusions. External standardization was done with the USGS GSD-1G standard, and the SRM612 standard was measured as an unknown for quality control in the absence of a well-characterized epidote standard. Bracketing standardization enabled a true-time linear drift correction. Data reduction was carried out with the software SILLS (Guillong et al., 2008), using the sum of total oxides minus H_2O (98.3 % for epidote and 100 % for SRM612) as an internal standard (see Halter et al., 2002). The formulation of Pettke et al. (2012) was employed to calculate limits of detection for each element in every analysis.

4.4 Pb isotope data

Measurements of ^{207}Pb / ^{206}Pb ratios (as well as ^{87}Sr / ^{86}Sr ratios; Sect. 4.5) were made in epidote micro-separates following the procedure for sample digestion in acids and for column chemistry detailed by Peverelli et al. (2021; modified from Nägler and Kamber, 1996). Two epidote micro-separates – each mixing Epidote-A (epidote in layer 1) and Epidote-B (epidote grains in the microfold in layers 2–3; see Sect. 5.1) in unknown and different proportions – were prepared (Ep_A + B_ 1 and Ep_A + B_2). After handpicking, the material was finely ground and washed with Milli-Q™ water. Two aliquots of each (Ep_A + B_1a and Ep_A + B_1b as well as Ep_A + B_2a and Ep_A + B_2b) were weighed in as replicates for each micro-separate, ensuring ca. 300 ng of Pb in each aliquot. During column chemistry with a Sr-spec™ resin (Horwitz et al., 1992), the Sr and Pb fractions were collected in sequence (Haeusler et al., 2016). One large Epidote-A grain was also handpicked and ground, and an amount of the powder corresponding to 250 ng of Sr was digested in acids before the extraction of the Sr fraction by column chemistry. The Pb fraction of this Epidote-A grain was not collected since Pb isotopic data are available from in situ U–Pb isotope measurements by LA-ICP-MS (Peverelli et al., 2021). Procedural blank samples were used to assess contamination during work in the laboratories. Lead isotope ratios were measured on a Thermo Fisher Neptune Plus MC-ICP-MS in desolvated plasma mode equipped with a CETAC Aridus 2 desolvating system. Instrumental mass fractionation was corrected within-run by means of a Tl spike. External reproducibility of the measurements was quantified by measuring the NIST NBS981 standard. The measured Pb isotope ratios were identical to those obtained by Rehkämper and Mezger (2000; their Table 4).

4.5 Strontium isotope data

Strontium isotope ratios were measured on a ThermoFisher Triton™ thermal ionization mass spectrometer (TIMS) after loading 250 ng Sr diluted in 6.4 M of HCl on Re filaments using 1.5 µL of a Ta-oxide activator. The SRM987 standard (200 ppm; Weis et al., 2006) was measured for quality control. The detected masses were 84, 85, 86 (center cup), 87, and 88. The interference of ^{87}Rb and within-run mass fractionation were corrected for by using the IUPAC ^{87}Rb / ^{85}Rb and ^{88}Sr / ^{86}Sr values of, respectively, 0.385617 and 8.735209. The SRM987 standard returned a weighted average ^{87}Sr / ^{86}Sr ratio of 0.710279 ± 0.000020 (2 standard deviations, 2 SD; number of replicates $n = 12$), which is higher than the preferred reference value of 0.710248 (see Weis et al., 2006). Standards AGV-2 ($n = 1$) and GSP-2 ($n = 2$) of USGS were measured as unknowns for quality control and they returned ^{87}Sr / ^{86}Sr ratios of 0.704041 ± 0.000018 (2 standard errors, 2 SE) and 0.765202 ± 0.000008 (2 SE), respectively. These values are also higher than the preferred reference values of 0.703981 ± 0.00009 (2 SD) and 0.765144 ± 0.000075 (2 SD) for AGV-2 and GSP-2, respectively (see Weis et al., 2006). A correction based on the reference materials returning higher ^{87}Sr / ^{86}Sr values than their reference values would produce the same shift in all measured ^{87}Sr / ^{86}Sr ratios. Hence, we did not correct our data because only the variability among the samples is relevant in this study, while the interpretation of the absolute Sr isotope ratios is beyond the scope of this work. Rubidium concentrations were not measured, as a correction for ^{87}Rb-derived ^{87}Sr is not necessary in epidote. This is a valid approach because the incompatibility of Rb in the epidote crystal structure results in negligible Rb concentrations (see Frei et al., 2004; Feineman et al., 2007).

5 Results

5.1 Microstructural analysis

The different characteristics of epidote and its microstructures in layers 1–3 (Figs. 3–4) allow the distinction of epidote into Epidote-A and Epidote-B as illustrated below. The microstructural characteristics of epidote – described below – suggest different formation mechanisms between epidote in layer 1 and in layers 2–3.

5.1.1 Layer 1: veining and Epidote-A

Layer 1 is characterized by coarse (ca. 0.2–1.6 mm) epidote grains associated with smaller angular ones (ca. 20–200 µm). The coarser epidote grains (Figs. 4d and 5a–b) form clusters with random shape orientations or are found as isolated crystals. Larger epidote grains are often surrounded by the smaller angular epidote grains (Fig. 5c; red arrow) as a result of brittle grain size reduction upon deformation with brittle deformation behavior of epidote. Epidote is euhedral to anhedral. Anhedral/subhedral epidote has lobate grain boundaries (Fig. 5d), and smaller epidote crystals are found in the gaps among the larger ones as well ("Ep clasts" in Fig. 5d). Quartz is mostly dynamically recrystallized, although some large quartz relicts are present, displaying undulose extinction (Fig. 5a–b). Hereafter, we refer to epidote in layer 1 as Epidote-A.

5.1.2 Layers 2–3: microfold and Epidote-B

In layers 2–3, the spatial distribution and the variable modal abundance of epidote define a fold (Figs. 3, 4b, 6, and A1). Smaller epidote grains with a shape-preferred orientation and quartz define axial planes (rectangle "a" in Fig. 3 and Figs. 4a and 6). Epidote grain boundaries are mostly curved and irregular, but a few subhedral or euhedral epidote grains are also observed (Fig. 6a, red arrow). Epidote grains vary between 5–90 µm in size, hampering U–Pb dating of epidote in layers 2–3. The modal abundance of epidote varies between ca. 5 vol. % and ca. 40 vol. % within the layer (Table 1), defining a quartz-supported microstructure. Where epidote is most abundant, quartz is confined as anhedral enclosures among epidote grains (Figs. 4b and 6b–c). Small (ca. 1–20 µm in size) oval epidote grains and fluid inclusions are observed within quartz grains (Fig. 6b–c). The size of dynamically recrystallized quartz grains correlates with grain size and abundance of epidote (Fig. 7). Such a relation, referred to as "Zener relation", shows interplay of grain sizes and related energies and deformation mechanisms occurring in epidote and quartz simultaneously (see Herwegh et al., 2011; and references therein). Dynamic recrystallization of quartz occurs by subgrain rotation (Figs. 4a–c and 7; compare with Stipp et al., 2002), leading to a crystallographic preferred orientation (CPO; Fig. 8a). The investigated layers show almost complete recrystallization, as indicated by the predominance of high boundary misorientations among quartz grains (Fig. 8b). The CPO shows a weak *c*-axis single girdle with related *a*-axis distribution, but also relicts of a cross-girdle can be inferred (Fig. 8c–d). These CPOs are interpreted as basal and rhomb slip systems as seen in Schmid and Casey (1986, and references therein) and Law (2014, and references therein). As discussed by Schmid and Casey (1986), the change from cross-girdle *c*-axis distribution towards a single girdle is related to the symmetry of deformation. Therefore, the *c* axes developed during pure and simple shear deformation, which is already documented in the microstructure (shearing and folding). A few quartz relicts are recognized thanks to their undulose extinction (black arrows in Figs. 4a, c, and A1). Where minor epidote is present, anhedral epidote grains of few micrometers to ca. 10 µm in size are most frequently interstitial and found at triple junctions among quartz subgrains (Fig. 9). We refer to subhedral to anhedral epidote grains in the microfold in layers 2–3 as Epidote-B.

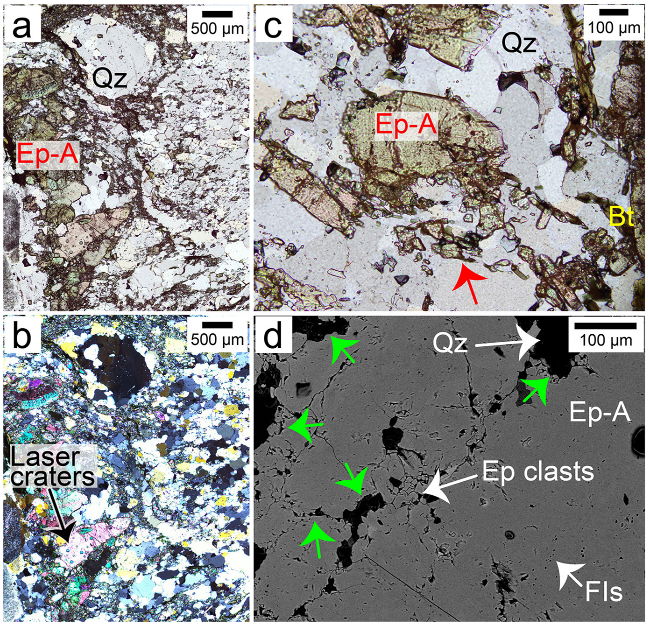

Figure 5. Details of epidote in layer 1. **(a–b)** Transmitted-light microphotographs of epidote and quartz in plane-polarized **(a)** and cross-polarized **(b)** light. **(c)** One isolated epidote grain surrounded by epidote clasts (red arrow). **(d)** Backscattered electron image of one epidote grain showing lobate grain boundaries and microporosity suggested by the presence of fluid inclusions (FIs). Bt: biotite; Ep: epidote; Ep-A: Epidote-A; Qz: quartz. Anomalous birefringence in panels **(a)** and **(c)** is due to the thickness of the thin section (ca. 60 µm).

5.2 Major and minor elements

The compositional maps in Fig. 10 (locations shown in Fig. 3) include layers 1–3, as marked in the figure. The

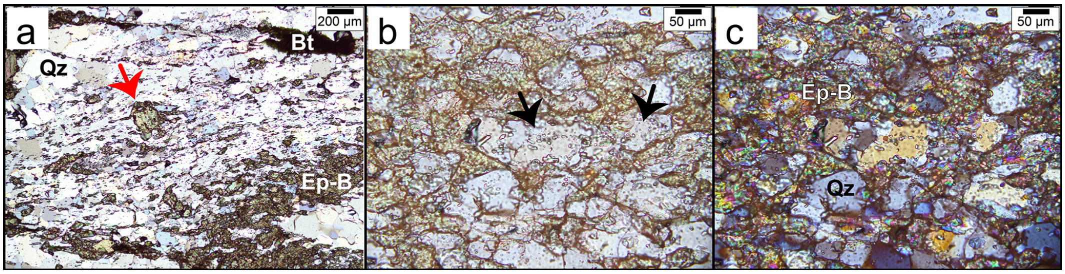

Figure 6. Transmitted-light microphotographs of layer 2. **(a)** Detail of the epidote microfold, with oval epidote grains hosted by dynamically recrystallized quartz and their long axes oriented consistently with the microfold axial planes. Red arrow: euhedral epidote grain. Overlapped images in plane-polarized and cross-polarized light. **(b–c)** Details of quartz enclosures among epidote grains in plane-polarized **(b)** and cross-polarized **(c)** light. The black arrows point at epidote and fluid inclusions in quartz. Bt; biotite; Ep-B: Epidote-B; Qz: quartz.

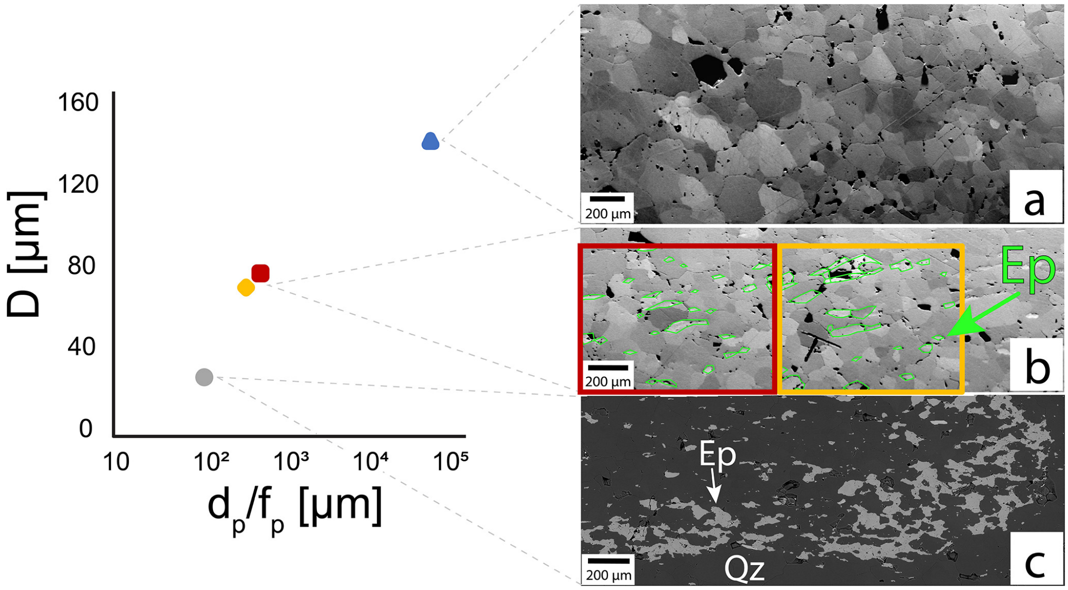

Figure 7. Correlation between quartz grain size (D) and Zener parameter (ratio between size and abundance of the second phase, here epidote, p; $\mathrm{d}p/\mathrm{f}p$) of epidote as the second phase determined in the FSE and BSE images of the microstructures in the microfold of layers 2–3. The green lines in the central BSE image contour epidote grains. Ep: epidote; Qz: quartz. Panels **(a)**, **(b)**, and **(c)** correspond, respectively, to Fig. 4c, a, and b.

compositions of FeO and Mn range between ca. 12.5 wt %–14 wt % and ca. 2500–5000 µg g^{-1}, respectively, across all analyzed epidote grains. On the one hand, larger Epidote-A grains in layer 1 are zoned, with FeO and Mn concentrations increasing from core to rim. Epidote in layers 2–3, on the other hand, is characterized by uniform concentrations of FeO and Mn. It should be noted that, because the step size of the compositional maps is 4 µm, the chemical variability in epidote in layers 2–3 is better assessed among different grains across the overall microstructure rather than within each crystal (i.e., the majority of grains do not contain enough 4 × 4 µm pixels).

5.3 Trace elements

The minimum spot size used for trace element measurements by LA-ICP-MS is 20 µm, which is ca. 4 times larger than the smallest epidote grains. Therefore, chemical variability is assessed throughout each microstructural layer by relying on measurements in large-enough epidote grains to avoid contamination from grain boundaries. Epidote-A is also addressed here with no specific reference to intra-grain zoning but only across the overall Epidote-A microstructure (i.e., layer 1). Data of Epidote-B are collected in anhedral epidote grains in layer 2. The different extents of chemical variability between Epidote-A and Epidote-B noted in the compositional maps (Fig. 10) are reflected by trace element data (Fig. 11, Table 2).

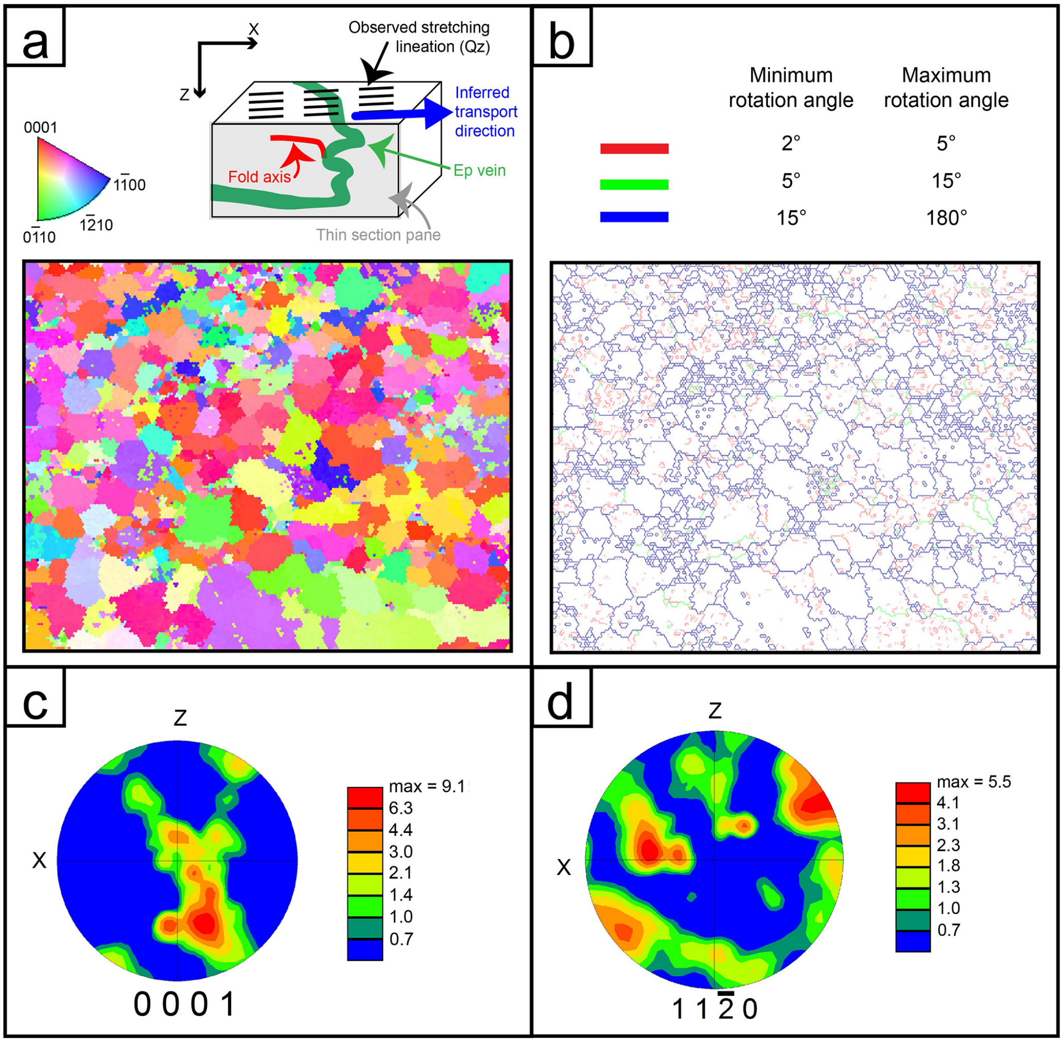

Figure 8. Crystallographic data of quartz in layer 3. (**a**, top part). The transpressional deformation produces shearing with some lineation (interpreted as transport direction). The related fold axes are oblique (and possibly curved) to the transport direction and cannot be properly described in 3D. The sketch should illustrate the orientation of the presented axes as shown in panels **(c)** and **(d)**. **(a)** Orientation of quartz grains in layer 3 (pure quartz area); colors correspond to the inverse pole figure shown on top. **(b)** Misorientation data of the area of panel **(a)**; note the dominant high-angle grain boundaries and some minor low-angle boundaries as developed after complete recrystallization, which is indicated by the CPO (shown in **c** and **d**). **(c)** Pole figure of quartz *c* axis, indicating a single girdle with relicts of a cross-girdle. **(c)** The *a* axes showing the classical distribution of rhomb and basal glide.

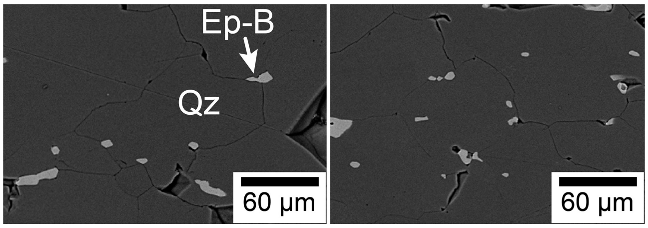

Figure 9. Backscattered electron images showing Epidote-B (Ep-B) grains along quartz (Qz) grain boundaries and at triple junctions among quartz grains.

The concentrations of Sr and Pb in Epidote-B overlap with the trend defined by the same elements measured in Epidote-A, but they cover a more limited range of values (Fig. 11a). The CI chondrite-normalized rare earth element (REE) patterns (Fig. 11b) of Epidote-A and Epidote-B have similar trends, characterized by positive slopes (La_N / Yb_N of 0.1–0.4 in Epidote-A and 0.03–0.5 in Epidote-B) and variably positive Eu anomalies (1.5–2.4 in Epidote-A and 1.2–2.3 in Epidote-B). The REE trends of Epidote-B fall within the range of Epidote-A and confirm the lesser extent of chemical variability in Epidote-B relative to Epidote-A. Selected elements, plotted as values normalized to the concentrations in the vein's host Central Aar Granite in Fig. 11c, reinforce chemical affinity between Epidote-A and Epidote-B, as well as the lesser chemical variability in the latter relative to the former. Cathodoluminescence (CL) images of the recrystallized quartz grains (Fig. 12) qualitatively indicate trace element variability also in quartz grains (see Ramseyer et al., 1988; Götze et al., 2001; Nègre et al., 2022).

5.4 Isotope data

Strontium and Pb isotopic data (Table 3) of the epidote micro-separates and those of the Epidote-A grain are plotted in Fig. 13. To compare the Pb and Sr isotopic composition of Epidote-A with those of the micro-separates mixing Epidote-A and Epidote-B, data obtained from three different techniques are combined in one $^{207}\mathrm{Pb} / ^{206}\mathrm{Pb}$-versus-$^{87}\mathrm{Sr} / ^{86}\mathrm{Sr}$ plot. All $^{87}\mathrm{Sr} / ^{86}\mathrm{Sr}$ ratios and the $^{207}\mathrm{Pb} / ^{206}\mathrm{Pb}$ ratios of the micro-separates mixing Epidote-A and Epidote-B were measured by bulk techniques – namely TIMS and solution ICP-MS – which homogenize ca. 9×10^9 µm^3 of epidote material. Epidote-A $^{207}\mathrm{Pb} / ^{206}\mathrm{Pb}$ ratios are taken from LA-ICP-MS measurements by Peverelli et al. (2021), which include 23 in situ analyses sampling ca. 20–24 $\times 10^3$ µm^3 each. The small volume of epidote material sampled in LA-ICP-MS analyses causes much larger variation among the single $^{207}\mathrm{Pb} / ^{206}\mathrm{Pb}$ analyses. In order to plot one datum point for each micro-separate aliquot against one representing the Epidote-A end-member, an average $^{207}\mathrm{Pb} / ^{206}\mathrm{Pb}$ ratio has to be calculated from the LA-ICP-MS data points. To obtain one datum point for Epidote-A, thus, we use analysis no. 10 of Peverelli et al. (2021; see their Table 5) to represent the $^{207}\mathrm{Pb} / ^{206}\mathrm{Pb}$ ratio of Epidote-A in combination with the $^{87}\mathrm{Sr} / ^{86}\mathrm{Sr}$ ratio measured by TIMS (Table 3). This is the datum point closest to the average (0.786) and to the median (0.787) values of the $^{207}\mathrm{Pb} / ^{206}\mathrm{Pb}$ ratios measured by LA-ICP-MS, hence the best representative value of $^{207}\mathrm{Pb} / ^{206}\mathrm{Pb}$ in Epidote-A. It should be noted that there is a fundamental difference between the Pb and Sr isotope systems in epidote: Sr isotopes reflect the Sr isotope composition of the fluid, given the negligible Rb contents of epidote. In contrast, the measured $^{207}\mathrm{Pb} / ^{206}\mathrm{Pb}$ ratios contain both initial (i.e., inherited from the fluid during crystallization) and radiogenic (i.e., ingrown and U-derived after crystallization) Pb. Therefore, Fig. 13 is a plot of total (initial + radiogenic) $^{207}\mathrm{Pb} / ^{206}\mathrm{Pb}$ vs. initial $^{87}\mathrm{Sr} / ^{86}\mathrm{Sr}$ ratios.

6 Discussion of the formation mechanisms for the epidote–quartz microfold

6.1 Interplay of epidote dissolution–precipitation and quartz dynamic recrystallization

The formation of a hydrothermal vein entails the crystallization of a mineral assemblage from a mineralizing fluid that fills a fracture (Bons et al., 2012). Although the original morphology of the studied epidote–quartz vein is obliterated by deformation, the euhedral, often elongate, shapes of Epidote-A grains (Fig. 4d) suggest that the formation of Epidote-A in layer 1 is related to vein-filling mineralization, with crystallization occurring in equilibrium with a fluid as observed in less deformed epidote veins (e.g., Fig. 1a and c of Peverelli et al., 2021) and in other vein-filling minerals (e.g., Oliver and Bons, 2001; Bons et al., 2012; and references therein). The reasons why layer 1 is less deformed than layers 2–3 may be linked to the closer proximity of layer 1 to the host rock, to a role of mechanically strong epidote clusters forming a load-bearing network, or to a combination of both (Handy, 1990, 1994; Masuda, 1990, 1995; Tullis, 2002; Passchier, 2005). The microstructures in layers 2–3 differing from those in layer 1 (Sect. 5.1), along with the lesser extent of chemical variability across epidote grains in layers 2–3 compared to Epidote-A in layer 1 (Figs. 10–11), suggest that the mechanism of formation of Epidote-B is different than that of Epidote-A. The Zener relation between quartz and epidote in layers 2–3 indicates an interplay between epidote and quartz during the formation of this microstructural domain. At the same time, the alignment of Epidote-B grains along the axial planes (Figs. 4a and 6) and the presence of minute Epidote-B crystals along grain boundaries of dynamically recrystallized quartz grains (Fig. 9) suggest that quartz dynamic recrystallization and Epidote-B formation are linked processes and thus that Epidote-B formed during deformation. The overlap in major and trace element compositions of Epidote-B and Epidote-A (Figs. 10–11), though, demonstrates that these epidote generations are chemically related. One way to reconcile this geochemical affinity with different formation mechanisms is a scenario in which Epidote-B formed via dissolution of Epidote-A grains and (re)precipitation during deformation. In fact, a few euhedral epidote grains can still be recognized in layer 2 (Fig. 6a), which are interpreted as Epidote-A relicts inherited from the original vein morphology. The gradation from epidote-rich/quartz-poor domains to virtually epidote-free/quartz-dominated ones in layers 2–3 (Figs. 3, 4, 6a, 7, and 14g) suggests that veining processes produced a morphology similar to that shown in Fig. 14a and that the original vein microstructure was subsequently deformed to form the present-day epidote–quartz spatial distribution. In fact, shifts between epidote-rich and quartz-rich domains are frequent in epidote–quartz veins (e.g., Fig. 1a and c in Peverelli et al., 2021). Further evidence for fluid-mediated mass transfer is also given by CL images of quartz

Table 2. Trace element composition of epidote measured by LA-ICP-MS (µg g^{-1}).

Epidote-A

Spot	Ba	Sr	Pb	U	La	Ce	Pr	Nd	Sm	Eu	Gd	Tb	Dy	Y	Ho	Er	Tm	Yb	Lu	Zr	V
1	0.99	1400	130	79	5.6	14	2.2	12	6.3	3.9	14	2.8	22	200	5.5	19	2.7	19	2.7	3.6	140
2	1.2	1990	130	130	7.7	18	2.7	15	8.5	5.6	18	3.6	27	230	6.4	22	3.1	21	3.4	5.1	140
3	22	3290	150	350	4.8	8.8	1.2	5.6	2.5	2.0	5.7	1.2	12	120	3.6	14	2.5	21	3.8	22	110
4	21	2500	170	270	0.99	1.9	0.24	1.1	0.66	1.1	2.8	0.86	9.8	110	3.1	14	2.7	23	4.4	24	110
5	1.9	970	97	60	5.2	9.3	1.1	5.0	1.8	1.3	2.9	0.62	5.1	32	1.0	3.5	0.53	3.7	0.57	4.2	160
6	23	2590	170	130	10	15	1.6	7.0	2.8	1.9	5.6	1.3	9.9	71	2.3	9.2	1.6	15	3.1	51	130
7	0.98	740	87	140	5.0	9.3	1.2	5.3	2.7	1.6	5.5	1.1	8.4	53	1.8	6.0	0.88	5.8	0.77	4.5	200
8	21	2870	170	240	12	17	1.8	8.3	4.6	3.7	11	2.5	19	130	4.4	17	2.8	25	4.4	17	150
9	9.7	2000	150	100	8.5	12	1.4	5.9	3.2	2.7	8.0	1.8	14	82	2.9	8.7	1.1	7.8	1.3	9.6	140
10	24	2890	170	220	6.6	9.7	1.1	4.6	2.0	2.2	5.9	1.4	12	90	2.9	11	2.1	18	3.2	31	140
11	0.92	1660	93	100	3.4	7.2	0.90	3.3	1.2	1.4	2.7	0.59	5.1	41	1.3	4.1	0.42	2.5	0.28	2.2	110
12	34	3750	190	140	5.3	8.5	1.0	4.6	1.9	2.3	4.2	1.0	8.8	67	2.2	6.7	0.80	4.8	0.64	25	120
13	0.59	770	78	160	1.6	3.0	0.39	1.6	1.0	1.5	3.2	1.0	9.1	65	2.2	7.9	0.97	5.9	0.72	3.2	180
14	27	2820	180	260	1.3	2.5	0.29	1.2	1.2	1.5	4.6	1.3	12	120	3.5	14	2.8	28	4.6	42	130
15	5.8	1530	93	54	0.62	0.97	0.12	0.62	0.45	0.94	1.4	0.40	4.1	42	1.2	4.7	0.77	6.2	1.0	5.0	140
16	17	2810	150	140	1.9	3.0	0.35	1.4	0.55	1.3	1.7	0.66	7.8	77	2.3	9.3	1.6	14	2.3	18	130
17	5.2	1310	93	120	3.5	6.3	0.78	3.7	1.3	1.4	2.0	0.57	4.9	47	1.3	6.1	0.88	7.1	0.93	5.2	120
18	3.8	2340	110	110	1.5	2.9	0.43	1.6	0.76	1.2	1.6	0.47	4.9	47	5.5	5.5	0.78	5.8	0.90	3.1	120

Epidote-B

Spot	Ba	Sr	Pb	U	La	Ce	Pr	Nd	Sm	Eu	Gd	Tb	Dy	Y	Ho	Er	Tm	Yb	Lu	Zr	V
1	2.1	1640	171	130	4.7	10	1.4	7.1	3.4	3.0	7.3	1.7	16	150	4.4	14	2.1	14	2.3	5.2	130
2	2.9	1860	150	140	3.7	8.1	1.1	5.7	3.1	3.1	7.6	2.1	17	170	4.6	16	2.4	19	3.0	5.9	140
3	6.6	1950	120	190	1.7	4.2	0.55	2.9	1.2	1.6	3.1	0.81	8.1	85	2.1	8.6	1.5	9.7	1.7	8.2	120
4	5.0	1720	140	190	3.3	7.6	1.1	5.2	2.4	2.0	4.8	1.1	10	110	3.1	11	1.8	13	2.1	7.0	120
5	4.2	1700	130	170	3.0	7.4	0.97	5.0	2.3	2.1	4.2	1.2	11	120	3.0	11	2.0	14	2.5	7.7	120
6	5.1	1930	120	160	1.9	4.4	0.60	2.9	1.4	1.5	3.3	0.80	7.4	85	2.3	8.8	1.3	10	1.6	7.2	130
7	3.7	1530	130	160	2.9	6.6	0.88	4.5	2.1	1.7	4.1	0.73	7.9	84	2.3	8.3	1.3	9.0	1.6	5.2	130
8	6.5	1960	140	190	3.3	7.6	0.99	4.5	2.3	1.9	3.9	0.99	9.1	100	2.6	10	1.5	13	2.1	9.3	130
9	5.3	1850	130	190	3.4	8.2	1.1	4.7	2.2	1.9	3.7	0.91	8.4	100	2.7	9.9	1.5	13	2.1	8.6	130
10	5.4	1800	130	190	2.3	5.2	0.71	3.5	1.7	1.7	3.6	0.85	8.5	90	2.4	10	1.7	12	2.2	8.1	130
11	5.5	1800	150	180	3.9	8.5	1.2	5.6	2.5	1.9	4.9	0.99	9.8	100	2.7	10	1.6	12	1.9	8.0	130
12	4.8	1710	151	230	9.4	20	2.6	12	5.3	3.5	9.6	2.3	19	160	4.8	16	2.4	16	2.6	7.6	130

Central Aar Granite (Schaltegger and Krähenbühl, 1990)

KAW 2219	Ba	Sr	Pb	U	La	Ce	Pr	Nd	Sm	Eu	Gd	Tb	Dy	Y	Ho	Er	Tm	Yb	Lu	Zr	V
2219	430	75	24	8	26	61	—	-	5.1	0.51	–	2.4	–	56	–	–	–	8.6	12	192	18

Table 3. Pb and Sr isotope data by solution ICP-MS and TIMS. Uncertainties are 2 standard errors (2 SE).

	^{207}Pb / ^{206}Pb	2 SE	^{87}Sr / ^{86}Sr	2 SE
Ep_A + B_1a	0.79159	0.00001	0.727803	0.000011
Ep_A + B_1b	0.79108	0.00001	0.727807	0.000007
Ep_A + B_2a	0.79428	0.00001	0.726952	0.000010
Ep_A + B_2b	0.79391	0.00001	0.726830	0.000015
Epidote-A	0.7867*	0.0058*	0.726552	0.000007

* Datum point no. 10 of Peverelli et al. (2021; their Table 5) by LA-ICP-MS.

(Fig. 12): these indicate trace element variability within single quartz grains, which is most likely the result of recrystallization in the presence of a fluid that mediated mass-transfer processes (e.g., Ramseyer et al., 1988; Götze et al., 2001; Nègre et al., 2022). The presence of a fluid during deformation is also supported by fluid inclusions in dynamically recrystallized quartz (Fig. 6b–c).

The transport of dissolved epidote-forming material towards the microfold axial planes (Fig. 14d) calls for a mechanism allowing the fluid to move throughout the deforming microstructural domain. The presence of ca. 10 µm sized Epidote-B grains along quartz grain boundaries and at triple junctions (Fig. 9) implies that dissolved epidote-forming material is transported and precipitated into locations of the new small Epidote-B sites. This is achieved by the presence of an interconnected network of porosity hosting an intergranular fluid that allows mass transfer processes. Although transport of dissolved epidote material may be possible by diffusion through an interconnected porosity network, fluid circulation at the centimeter scale enabling mass transfer processes is possible by cavitation with the formation of nucleation sites (Fig. 14e–f; also described as "dynamic granular fluid pump"; see Fusseis et al., 2009; Menegon et al., 2015) among sliding dynamically recrystallized quartz grains (Figs. 9 and 12). A first deformation step in which quartz grain size is reduced by dynamic recrystallization via subgrain rotation (Fig. 14c) is suggested by a crystallographic preferred orientation in quartz-dominated domains (Fig. 8). Once the new quartz grains are formed, grain boundary sliding produces creep cavities (Fig. 14e–f; see Herwegh and Jenni, 2001; Fusseis et al., 2009; Gilgannon et al., 2017, 2021), thus creating nucleation loci for Epidote-B (Fig. 9). A similar process is described by Gottardi and Hughes (2022) in quartzites deformed at the brittle–ductile transition in the crust, in which fluid inclusions are redistributed in the quartz matrix by dynamic recrystallization of quartz by subgrain rotation and grain boundary migration. A similar microstructure and a similar interplay of processes are also discussed in mafic high-temperature mylonites (Kruse and Stünitz, 1999) and quartzites (Nègre et al., 2021; Pongrac et al., 2022). This first step is followed by one in which the grain size and volume abundance of the newly precipitated Epidote-B grains control the grain size of quartz (Fig. 7), hence exerting control on quartz deformation mechanisms by pinning the migrating quartz boundaries (see Jessel, 1987; Olgaard, 1990; Humphreys and Ardakani, 1996; Bate, 2001; Herwegh and Berger, 2004; Herwegh et al., 2011; Cyprych et al., 2016). This suggests a feedback process: (1) quartz grain boundary sliding creates creep cavities in which Epidote-B crystallizes, (2) Epidote-B keeps quartz grain size small, (3) more creep cavities are formed, and (4) more Epidote-B grains are formed. This process is referred to as viscous granular flow (e.g., Fitz Gerald and Stünitz, 1993; Stünitz and Fitz Gerald, 1993; Paterson, 1995; see also Kruse and Stünitz, 1999). The dissolution of epidote may have been facilitated by increased surface area achieved via brittle grain size reduction in Epidote-A grains (Figs. 5c–d and 14b).

6.2 Open-system conditions and external fluids

Epidote dissolution–precipitation and the transport of dissolved epidote material to the loci of Epidote-B crystallization imply the presence of a fluid whose nature can be assessed by Pb–Sr isotope data. We have mentioned that the epidote micro-separates used for solution ICP-MS measurements mix Epidote-A and Epidote-B to unknown proportions, since the mechanical separation of pure Epidote-B is not feasible due to its small grain size. Therefore, the observation that the ^{207}Pb / ^{206}Pb and ^{87}Sr / ^{86}Sr ratios of the micro-separates are different (Fig. 13) suggests that the micro-separates include different epidote generations and hence that Epidote-A and Epidote-B crystallized from fluids with different Pb and Sr isotope compositions. This is supported by the Pb–Sr isotopic ratios of the micro-separates being different than that measured in an Epidote-A grain (Fig. 13, Table 2). There are two principal processes that can induce changes in the Pb and Sr isotope compositions: (1) radioactive decay of ^{235,238}U into ^{207,206}Pb and ^{87}Rb into ^{87}Sr or (2) open-system conditions allowing for advection of extraneous Pb and Sr with different isotopic compositions. Process (1) is unlikely in this case because ingrown radiogenic Pb and Sr would not be sufficient to cause the observed isotopic differences among micro-separates and Epidote-A grain (Fig. 13). Consequently, the Pb–Sr isotope heterogeneity of the two epidote generations infers fluid-mediated addition of extraneous Sr and Pb during crystallization of Epidote-B. Because the vein microstructure carries evidence of a single deformation event (Fig. 14g), it is likely that a second fluid type entered the system during vein deformation and formation of Epidote-B (Fig. 14d–f). Thus, the differences in Pb and Sr isotopic data of Epidote-A grain and micro-separates are interpreted to document mixing between different contributions: (1) one reflecting the isotopic composition of Epidote-A incorporated upon vein formation and (2) one reflecting the mixing of dissolved Epidote-A material with extraneous Pb and Sr brought to the site of Epidote-B crystallization. The existence of open-system conditions bears the potential for fluid-mediated transfer of chemical

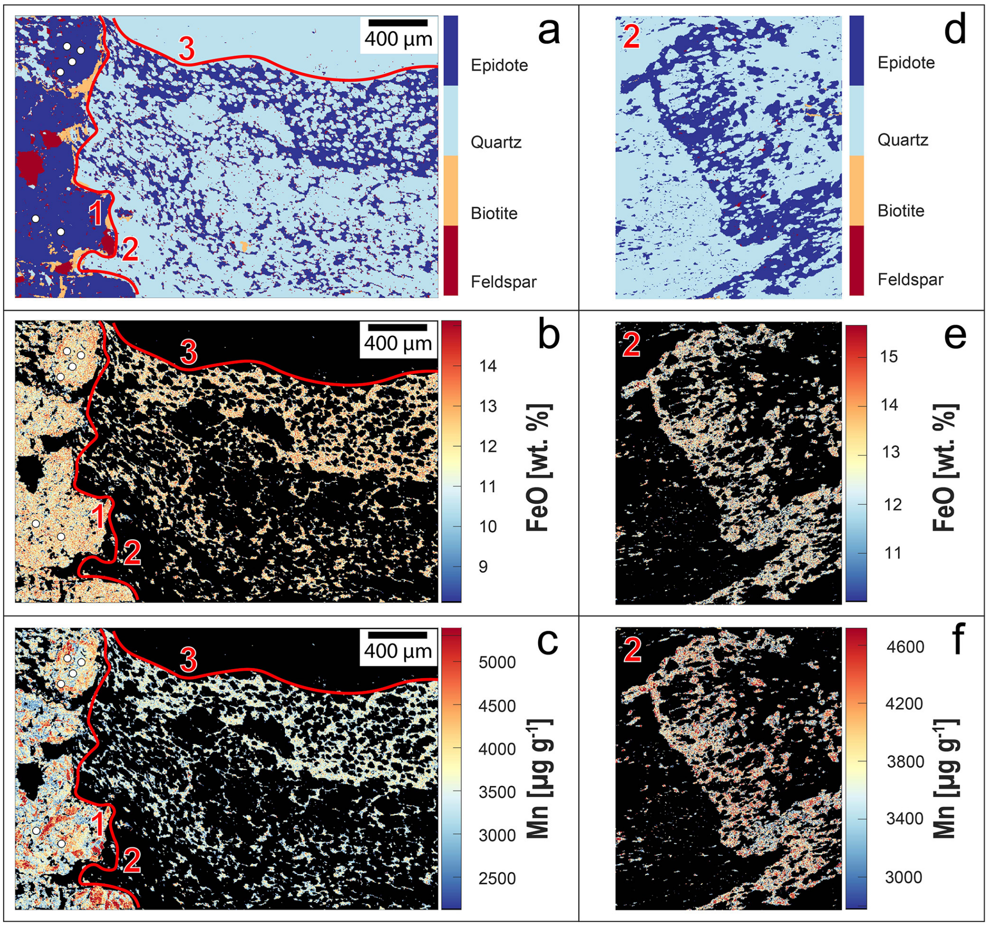

Figure 10. **(a–c)** Compositional maps across layers 1–3; white circles indicate spots for U–Pb dating by LA-ICP-MS of Peverelli et al. (2021). **(d–f)** Compositional maps of layer 2. For locations, see Fig. 3. Red numbers indicate vein layers, which are separated by the red curves. Scale bars in **(a–c)** also apply to **(d–f)**.

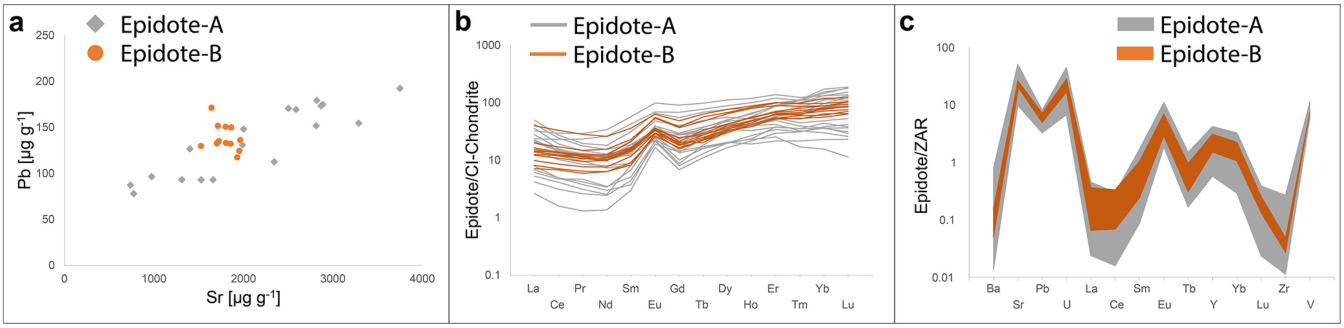

Figure 11. Epidote LA-ICP-MS data of **(a)** Pb and Sr mass fractions, **(b)** CI chondrite-normalized (McDonough and Sun, 1995) rare earth element (REE) patterns, and **(c)** mass fractions of selected trace elements in epidote normalized to the Central Aar Granite (ZAR; Schaltegger and Krähenbühl, 1990).

constituents (Fig. 14e–f). The fact that the major and trace element composition of Epidote-B maintains the same patterns as, and represents a narrower range of, that of Epidote-A (Figs. 10–11) suggests similarly (either rock- or fluid-)buffered conditions. Hence, during fluid-mediated crystallization of Epidote-A and Epidote-B, physico-chemical (e.g., P, T, fO_2) conditions – thus fluid compositions – were closely comparable. The initial compositional variability in Epidote-A thereby became homogenized upon dissolution and crystallization into Epidote-B. Considering that the

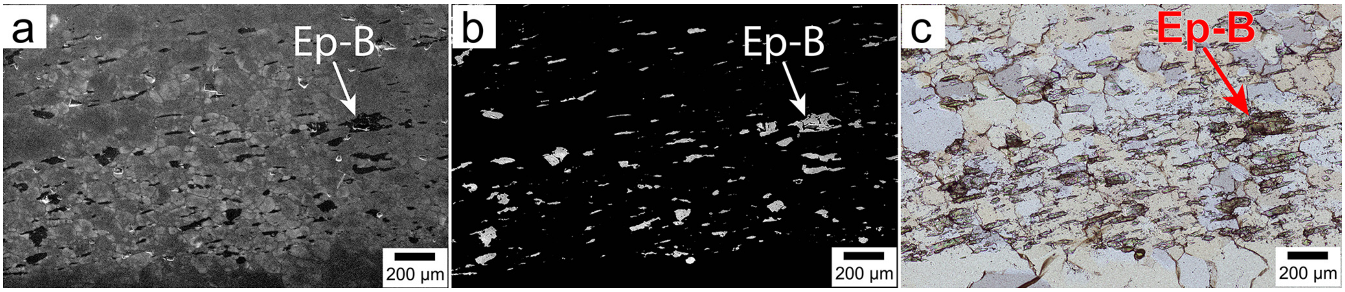

Figure 12. Cathodoluminescence (CL; **a**) and backscattered electron images **(b)** of the microstructural domain in the transmitted-light microphotograph of panel **(c)**. The only minerals in the images are epidote (Epidote-B; Ep-B) and quartz (unlabeled grains). The different CL contrasts in quartz **(a)** are due to variable trace element contents. The anomalous birefringence in panel **(c)** is due to the thickness of the thin section (ca. 60 µm).

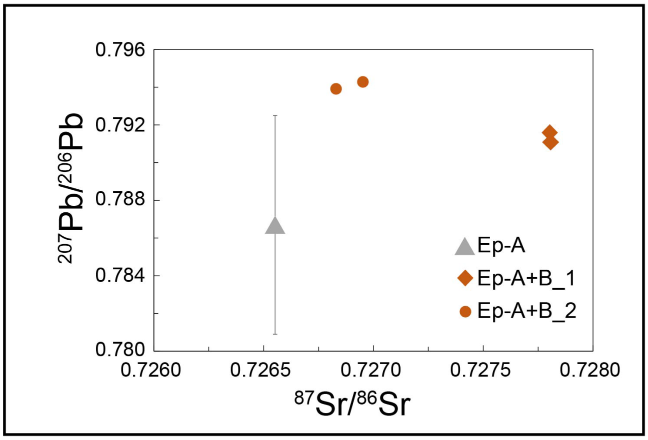

Figure 13. Total ^{207}Pb / ^{206}Pb and initial ^{87}Sr / ^{86}Sr data of Epidote-A (Ep-A) and epidote micro-separates (Ep-A + B_1 and Ep-A + B_2); the ^{207}Pb / ^{206}Pb ratio of Epidote-A is by LA-ICP-MS (analysis no. 10 of Peverelli et al., 2021; their Table 5); all other ^{207}Pb / ^{206}Pb ratios are by solution ICP-MS; ^{87}Sr / ^{86}Sr ratios are by TIMS; error bars are smaller than the symbols where not shown.

299 ± 2 Ma old host granitoid (Schaltegger and Corfu, 1992; Ruiz et al., 2022) contains minerals with high concentrations of U, Th, and Rb (e.g., allanite, biotite), even small and variable contributions of radiogenic Pb and Sr leached from these minerals may produce a measurable shift in Pb–Sr isotope ratios without a resolvable effect on Sr and Pb fluid concentrations. Also, crystallization of Epidote-A and Epidote-B most likely occurred under comparable T conditions (ca. 400–450 °C as inferred from the presence of biotite in the vein; see Goncalves et al., 2012). Hence, fluid–epidote partition coefficients of all measured elements remained similar between the two epidote crystallization events. Such a scenario can reconcile the compositional uniformity with Pb and Sr isotopic differences between Epidote-A and Epidote-B, hence allowing at least a fraction of the fluid involved in the deformation of layers 2–3 to be of external origin. Peverelli et al. (2022) measured the H isotope composition of epidote in this sample, obtaining values that can only be explained as a mixture of end-member waters (e.g., meteoric, seawater, etc.) as a source for the epidote-forming fluids. In light of the present data, it is possible that their measured δD value reflects the mixing of internal and external fluids upon deformation of the epidote–quartz vein as described above.

6.3 Epidote geochemistry as a result of veining vs. combined grain boundary sliding, cavitation, and nucleation

The present major and trace element data show that Epidote-B is geochemically similar to, and less variable than, Epidote-A (Figs. 10–11), and this result might be linked to differences in crystallization mechanisms between the two epidote generations. In a rock-dominated system, the larger geochemical variability in Epidote-A may be due to (1) fluid distillation during epidote crystallization, (2) slight variations in physico-chemical conditions (e.g., P, T) throughout the veining processes, or (3) pulsating fluid fluxes. Trace element data (Fig. 11a–b) defining trends and not distinct epidote populations suggest that the geochemical variability in Epidote-A is most readily explained by an evolving epidote-forming fluid chemistry along with more and more epidote precipitating, thus readily removing compatible elements from the fluid (see also Anenburg et al., 2015). This does not exclude multiple pulses of the same fluid (i.e., same fluid source and chemistry) and a role for varying physico-chemical conditions, such as small temperature variations (e.g., Trincal et al., 2015). The lesser extent of chemical variation in Epidote-B indicates homogenization of the whole trace element budget dissolved into the Epidote-B-forming fluid. Viscous granular flow is a dynamic process in which continuous feedback exists among dissolution of minerals, grain boundary sliding, creep cavitation, mass transfer, and mineral precipitation (e.g., Fitz Gerald and Stünitz, 1993; Stünitz and Fitz Gerald, 1993; Paterson, 1995). This implies that repeated dissolution and reprecipitation of the same material is likely to occur, and the chemical budget gets com-

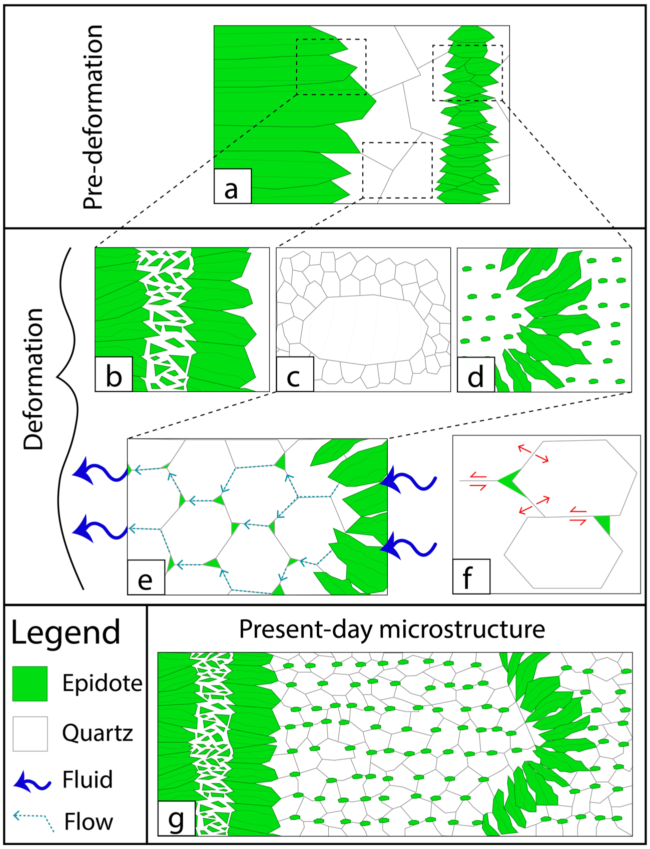

Figure 14. Sketches of the sequence of events affecting the studied epidote vein. **(a)** Original microstructure formed upon veining. **(b)** Detail of the fracturing occurring in Epidote-A in layer 1. **(c)** Dynamic recrystallization of quartz by subgrain rotation. **(d)** Folding of the epidote band in layer 2 and dissolution–precipitation forming Epidote-B. **(e)** Detail of the viscous granular flow process, cavitation, and formation of nucleation sites ("dynamic granular fluid pump" of Fusseis et al., 2009) allowing Epidote-B to precipitate in creep cavities along quartz grain boundaries. **(f)** Detail of quartz grain boundary sliding allowing dynamic granular fluid pump (modified from Fusseis et al., 2009). **(g)** Present-day microstructure. Not to scale.

positionally homogenized with ongoing deformation. Consequently, in the case of the epidote–quartz microfold in layers 2–3, such a mechanism may account for the chemical homogeneity of Epidote-B. In this respect, combined grain boundary sliding, cavitation, and nucleation promote recycling and homogenization of fluids in deforming polymineralic aggregates.

7 Consequences for epidote U–Pb ages

The inevitable question arising from the scenario developed above is what the U–Pb age measured in Epidote-A reflects. Temperature-driven resetting of the U–Pb system is excluded based on the peak temperature reached in the area (i.e., 450 ± 30 °C; Challandes et al., 2008; Goncalves et al., 2012) never exceeding the closure temperature for Pb diffusion in epidote (i.e., >685 °C; Dahl, 1997). As a consequence, solid-volume diffusion does not have the potential to affect Epidote-A U–Pb ages. However, the U–Pb isotope system may be affected by dissolution–precipitation, as has been reported for many minerals (e.g., monazite; Tartèse et al., 2011; Williams et al., 2011; Seydoux-Guillaume et al., 2012; Grand'Homme et al., 2018). Fluid–rock interaction has been shown to affect other isotopic systems as well (e.g., K–Ar, B; Halama et al., 2014). The microstructural relationships between Epidote-A and biotite in layer 1 are consistent with both minerals forming together in Alpine times and before vein deformation. The U–Pb isotopic data presented in Peverelli et al. (2021) resolve a single generation of Epidote-A at the available analytical precision in a Tera–Wasserburg diagram, which plots $^{238}U/^{206}Pb$ vs. $^{207}Pb/^{206}Pb$ ratios (Tera and Wasserburg, 1972). If any isotopic heterogeneity had been caused by interaction with the deformation-related fluid, the crystal rims would be affected to a greater extent than the cores. However, U–Pb isotope measurements cover all chemically variable zones in Epidote-A (Fig. 10, white circles), and they define a single Tera–Wasserburg regression regardless of their proximity to cores or rims of the analyzed epidote grains. Moreover, the time-resolved $^{206}Pb/^{238}U$ ratios corrected for downhole fractionation display flat trends when corrected for zoning in initial Pb by applying a ^{208}Pb correction (see Fig. 5 of Peverelli et al., 2021). This means that there is no resolvable isotopic zoning across the ca. 10–12 µm crater depth of the LA-ICP-MS measurements. Finally, the trace element data (Figs. 10c and 11, Table 2) reveal preserved prominent chemical zoning. This supports the notion that the dissolution–precipitation processes during Epidote-B formation did not disturb the U–Pb isotope system in Epidote-A relicts to a noticeable extent at the available analytical precision.

8 Conclusions and outlook

This study combines microstructural and geochemical methods to investigate the formation mechanisms of an epidote–quartz microfold within an epidote–quartz (± biotite) vein. We have suggested the occurrence of epidote dissolution–precipitation and that this process coexists with quartz dynamic recrystallization, both contributing to grain size reduction in the system. The genetic link between epidote grains being dissolved and those being reprecipitated is revealed by the overlap of the major and trace element compositions of both generations. We have shown that fluid circulation at the scale of the thin section and the formation of epidote nucleation loci in the deforming system are enabled by a combination of grain boundary sliding, creep cavitation, and mass transfer. Repeated dissolution and (re)precipitation processes of epidote in creep cavities formed among sliding quartz grain boundaries also cause chemical homogenization of the epidote-dissolving and epidote-forming fluid and hence of the new epidote generation forming during deformation. This demonstrates the importance of fluid recycling in deformational processes, although the application of Pb–Sr isotope geochemistry recognizes a role for the addition of externally derived fluids mediating mass transfer processes in the studied epidote–quartz vein. Epidote plays an active role in determining the deformation behavior of other minerals and hence in the deformation style of polymineralic aggregates and in producing the resulting microstructures. To our knowledge, before this study, only brittle deformation behavior of epidote had been proven (Masuda et al., 1990, 1995), but no other detailed studies had addressed epidote deformation mechanisms. In this respect, although Stünitz and Fitz Gerald (1993) do not observe any plastic deformation in clinozoisite, epidote dynamic recrystallization has never been ruled out or demonstrated rigorously. However, since this mineral is widespread in crustal rocks (e.g., Bird and Spieler, 2004; Enami et al., 2004; Franz and Liebscher, 2004; Grapes and Hoskin, 2004; Schmidt and Poli, 2004; Morad et al., 2010), the occurrence of epidote ductile deformation may have effects on the deformation of the continental crust, and it calls for a better understanding of this mineral.

Appendix A

Transmitted-light microphotograph of the microfold in layers 2–3.

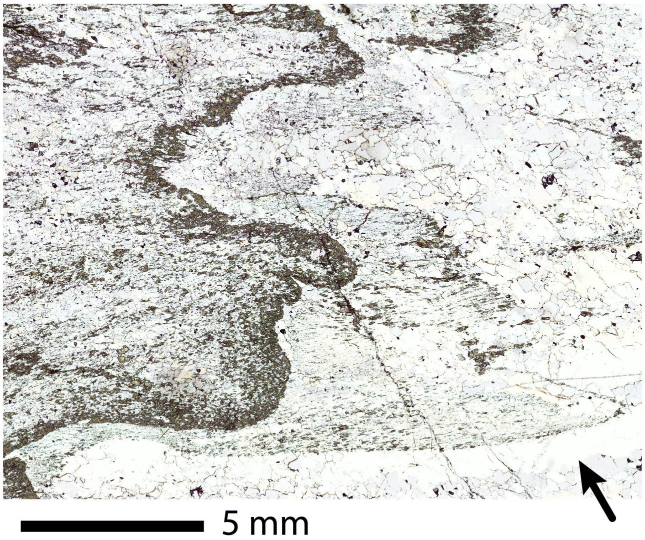

Figure A1. Transmitted-light scan of layers 2–3. Plane-polarized light.

Data availability. All new data are included in the paper (see Tables and Figures). U-Pb isotope data of Epidote-A are available in Table 5 of Peverelli et al. (2021; https://doi.org/10.5194/gchron-3-123-2021).

Author contributions. VP prepared the samples, carried out grain size analysis and petrographic description, planned electron microprobe work, ran trace element measurements by LA-ICP-MS, measured Sr isotopes by TIMS, and prepared the manuscript. AB and MH supervised the work and greatly contributed to structuring the manuscript. MW supervised clean lab work and TIMS analyses and measured Pb isotope data with IMV. TP granted access to the LA-ICP-MS laboratory and was closely involved in structuring the manuscript and in data evaluation. PL performed work at the electron microprobe and processed the X-ray maps. All authors read the manuscript and contributed to its improvement.

Competing interests. The contact author has declared that none of the authors has any competing interests.

Acknowledgements. The authors thank Florian Fusseis for handling the manuscript, as well as an anonymous reviewer, Holger Stünitz, and Matthias Konrad-Schmolke for their constructive reviews and feedback. We are also deeply thankful to Klaus Mezger for his unofficial review of the manuscript during revision and to Francesca Piccoli for technical assistance with LA-ICP-MS measurements and feedback on the work. We acknowledge funding of our new LA-ICP-MS facility through the Swiss National Science Foundation, project 206021_170722, to Daniela Rubatto and Thomas Pettke. The solution ICP-MS isotope data were obtained on a Neptune MC-ICP mass spectrometer acquired with funds from the NCCR PlanetS supported by the Swiss National Science Foundation (grant no. 51NF40-141881). This work is part of the PhD thesis of Veronica Peverelli, who acknowledges SNF funding (project no. 178785) granted to Alfons Berger.

Financial support. This research has been supported by the Schweizerischer Nationalfonds zur Förderung der Wissenschaftlichen Forschung (grant no. 178785).

Review statement. This paper was edited by Florian Fusseis and reviewed by Holger Stunitz, Matthias Konrad-Schmolke, and one anonymous referee.

References

Anenburg, M., Katzir, Y., Rhede, D., Jöns, N., and Bach, W.: Rare earth element evolution and migration in plagiogranites: a record preserved in epidote and allanite of the Troodos ophiolite, Contrib. Mineral. Petrol., 169, 25, https://doi.org/10.1007/s00410-015-1114-y, 2015.

Bambauer, H. U., Herwegh, M., and Kroll, H.: Quartz as indicator mineral in the Central Swiss Alps: The quartz recrystallization isograd in the rock series of the northern Aar massif, Swiss J. Geosci., 102, 345–351, https://doi.org/10.1007/s00015-009-1319-z, 2009.

Bate, P.: The effect of deformation on grain growth in Zener pinned systems, Acta Mater., 49, 1453–1461, https://doi.org/10.1016/S1359-6454(01)00033-7, 2001.

Belgrano, T. M., Herwegh, M., and Berger, A.: Inherited structural controls on fault geometry, architecture and hydrothermal activity: an example from Grimsel Pass, Switzerland, Swiss J. Geosci., 109, 345–364, https://doi.org/10.1007/s00015-016-0212-9, 2016.

Bergemann, C., Gnos, E., Berger, A., Whitehouse, M., Mullis, J., Wehrens, P., Pettke, T., and Janots, E.: Th-Pb ion probe dating of zoned hydrothermal monazite and its implications for repeated shear zone activity: An example from the central alps, Switzerland, Tectonics, 36, 671–689, https://doi.org/10.1002/2016TC004407, 2017.

Berger, A., Gnos, E., Janots, E., Whitehouse, M., Soom, M., Frei, R., and Waight, T. E.: Dating brittle tectonic movements with cleft monazite: Fluid-rock interaction and formation of REE minerals, Tectonics, 32, 1176–1189, https://doi.org/10.1002/tect.20071, 2013.

Berger, A., Mercolli, I., Herwegh, M., and Gnos, E.: Geological Map of the Aar Massif, Tavetsch and Gotthard Nappes, Geol. spec. Map 1 : 100000, explanatory notes 129, Federal Office of Topogaphy swisstopo, Bern, Switzerland, 2017a.

Berger, A., Wehrens, P., Lanari, P., Zwingmann, H., and Herwegh, M.: Microstructures, mineral chemistry and geochronology of white micas along a retrograde evolution: An example from the Aar massif (Central Alps, Switzerland), Tectonophysics, 721, 179–195, https://doi.org/10.1016/j.tecto.2017.09.019, 2017b.

Berger, A., Egli, D., Glotzbach, C., Valla, P. G., Pettke, T., and Herwegh, M.: Apatite low-temperature chronometry and microstructures across a hydrothermally active fault zone, Chem. Geol., 588, 120633, https://doi.org/10.1016/j.chemgeo.2021.120633, 2022.

Bird, D. K. and Spieler, A. R.: Epidote in Geothermal Systems, Rev. Mineral. Geochem., 56, 235–300, https://doi.org/10.2138/gsrmg.56.1.235, 2004.

Bons, P. D., Elburg, M. A., and Gomez-Rivas, E.: A review of the formation of tectonic veins and their microstructures, J. Struct. Geol., 43, 33–62, https://doi.org/10.1016/j.jsg.2012.07.005, 2012.

Bukovská, Z., Jeřábek, P., and Morales, F. G.: Major softening at brittle-ductile transition due to interplay between chemical and deformation processes: An insight from evolution of shear bands in the South Armorican Shear Zone, J. Geophys. Res.-Sol. Ea., 121, 1158–1182, https://doi.org/10.1002/2015JB012319, 2016.

Challandes, N., Marquer, D., and Villa, I. M.: P-T-t modelling, fluid circulation, and ^{39}Ar–^{40}Ar and Rb-Sr mica ages in the Aar Massif shear zones (Swiss Alps), Swiss J. Geosci., 101, 269–288, https://doi.org/10.1007/s00015-008-1260-6, 2008.

Choukroune, P. and Gapais, D.: Strain pattern in the Aar Granite (Central Alps): orthogneiss developed by bulk inhomogeneous flattening, J. Struct. Geol., 5, 411–418, https://doi.org/10.1016/b978-0-08-030273-7.50019-7, 1983.

Cyprych, D., Piazolo, S., Wilson, C. J. L., Luzin, V., and Prior, D. J.: Rheology, microstructure and crystallographic preferred orientation of matrix containing a dispersed second phase: Insight from experimentally deformed ice, Earth Planet. Sc. Lett., 449, 272–281, https://doi.org/10.1016/j.epsl.2016.06.010, 2016.

Dahl, P. S.: A crystal-chemical basis for Pb retention and fission-track annealing systematics in U-bearing mineral, with implications for geochronology, Earth Planet. Sc. Lett., 150, 277–290, https://doi.org/10.1016/S0012-821X(97)00108-8, 1997.

Diamond, L. W., Wanner, C., and Waber, H. N.: Penetration depth of meteoric water in orogenic geothermal systems, Geology, 46, 1083–1066, https://doi.org/10.1130/G45394.1, 2018.

Egli, D., Baumann, R., Küng, S., Berger, A., Baron, L., and Herwegh, M.: Structural characteristics, bulk porosity and evolution of an exhumed long-lived hydrothermal system, Tectonophysics, 747/748, 239–258, https://doi.org/10.1016/j.tecto.2018.10.008, 2018.

Enami, M., Liou, J. G., and Mattinson, C. G.: Epidote minerals in high P/T metamorphic terranes: Subduction zone and high- to ultrahigh-pressure metamorphism, Rev. Mineral. Geochem., 56, 347–398, https://doi.org/10.2138/gsrmg.56.1.347, 2004.

Evans, B., Renner, J., and Hirth, G.: A few remarks on the kinetics of static grain growth in rocks, Int. J. Earth Sci., 90, 88–103, https://doi.org/10.1007/s005310000150, 2001.

Feineman, M. D., Ryerson, F. J., DePaolo, D. J., and Plank, T.: Zoisite-aqueous fluid trace element partitioning with implications for subduction zone fluid composition, Chem. Geol., 239, 250–265, https://doi.org/10.1016/j.chemgeo.2007.01.008, 2007.

Ferreira, T. and Wayne, R.: ImageJ user guide, ImageJ/Fiji, 155–161, 2012

Fitz Gerald, J. D. and Stünitz, H.: Deformation of granitoids at low metamorphic grade, I: Reactions and grain size reduction., Tectonophysics, 221, 269–297, https://doi.org/10.1016/0040-1951(93)90163-E, 1993.

Franz, G. and Liebscher, A.: Physical and Chemical Properties of the Epidote Minerals – An Introduction, Rev. Mineral. Geochem., 56, 1–81, https://doi.org/10.2138/gsrmg.56.1.1, 2004.

Frei, D., Liebscher, A., Franz, G., and Dulski, P.: Trace element geochemistry of epidote minerals, Rev. Mineral. Geochem., 56, 553–605, https://doi.org/10.2138/gsrmg.56.1.553, 2004.

Fusseis, F., Regenauer-Lieb, K., Liu, J., Hough, R. M., and De Carlo, F.: Creep cavitation can establish a dynamic granular fluid pump in ductile shear zones, Nature, 459, 974–977, https://doi.org/10.1038/nature08051, 2009.

Gilgannon, J., Fusseis, F., Menegon, L., Regenauer-Lieb, K., and Buckman, J.: Hierarchical creep cavity formation in an ultramylonite and implications for phase mixing, Solid Earth, 8, 1193–1209, https://doi.org/10.5194/se-8-1193-2017, 2017.

Gilgannon, J., Waldvogel, M., Poulet, T., Fusseis, F., Berger, A., Barnhoorn, A., and Herwegh, M.: Experimental evidence that viscous shear zones generate periodic pore sheets, Solid Earth, 12, 405–420, https://doi.org/10.5194/se-12-405-2021, 2021.

Giuntoli, F., Menegon, L., and Warren, C. J.: Replacement reactions and deformation by dissolution and precipitation processes in amphibolites, J. Metamorph. Geol., 36, 1263–1286, https://doi.org/10.1111/jmg.12445, 2018.

Goncalves, P., Oliot, E., Marquer, D., and Connolly, J. A. D.: Role of chemical processes on shear zone formation: An example from the Grimsel metagranodiorite (Aar massif, Central Alps), J. Metamorph. Geol., 30, 703–722, https://doi.org/10.1111/j.1525-1314.2012.00991.x, 2012.

Gottardi, R. and Hughes, B.: Role of fluids on deformation in mid-crustal shear zones, Raft River Mountains, Utah, Geol. Mag., 159, 1–13, https://doi.org/10.1017/S0016756822000231, 2022.

Götze, J., Plötze, M., and Habermann, D.: Origin, spectral characteristics and practical applications of the cathodoluminescence (CL) of quartz – A review, Mineral. Petrol., 71, 225–250, https://doi.org/10.1007/s007100170040, 2001.

Grand'Homme, A., Janots, E., Seydoux-Guillaume, A. M., Guillaume, D., Magnin, V., Hövelmann, J., Höschen, C., and Boiron, M. C.: Mass transport and fractionation during monazite alteration by anisotropic replacement, Chem. Geol., 484, 51–68, https://doi.org/10.1016/j.chemgeo.2017.10.008, 2018.

Grapes, R. H. and Hoskin, P. W. O.: Epidote group minerals in low-medium pressure metamorphic terranes, Rev. Mineral. Geochem., 56, 301–345, https://doi.org/10.2138/gsrmg.56.1.301, 2004.

Guillong, M., Meier, D. L., Allan, M. M., Heinrich, C. A., and Yardley, B. W. D.: SILLS: A Matlab-Based Program for the Reduction of Laser Ablation ICP–MS Data of Homogeneous Materials and Inclusions, Mineral. Assoc. Can. Short Course, 40, 328–333, 2008.

Haeusler, M., Haas, C., Lösch, S., Moghaddam, N., Villa, I. M., Walsh, S., Kayser, M., Seiler, R., Ruehli, F., Janosa, M., and Papageorgopoulou, C.: Multidisciplinary identification of the controversial freedom fighter Jörg Jenatsch, assassinated 1639 in Chur, Switzerland, PLOS ONE, 11, e0168014, https://doi.org/10.1371/journal.pone.0168014, 2016.

Halama, R., Konrad-Schmolke, M., Sudo, M., Marschall, H. R., and Wiedenbeck, M.: Effects of fluid-rock interaction on 40Ar/39Ar geochronology in high-pressure rocks (Sesia-Lanzo Zone, Western Alps), Geochim. Cosmochim. Ac., 126, 475–494, https://doi.org/10.1016/j.gca.2013.10.023, 2014.

Halter, W. E., Pettke, T., Heinrich, C. A., and Rothen-Rutishauser, B.: Major to trace element analysis of melt inclusions by laser-ablation ICP-MS: Methods of quantification, Chem. Geol., 183, 63–86, https://doi.org/10.1016/S0009-2541(01)00372-2, 2002.

Handy, M. R.: The solid-state flow of polymineralic rocks, J. Geophys. Res.-Ea., 95, 8647–8661, https://doi.org/10.1029/JB095iB06p08647, 1990.

Handy, M. R.: Flow laws for rocks containing two non-linear viscous phases: A phenomenological approach, J. Struct. Geol., 16, 287–301, https://doi.org/10.1016/0191-8141(94)90035-3, 1994.

Hentschel, F., Janots, E., Trepmann, C. A., Magnin, V., and Lanari, P.: Corona formation around monazite and xenotime during greenschist-facies metamorphism and deformation, Eur. J. Mineral., 32, 521–544, https://doi.org/10.5194/ejm-32-521-2020, 2020.

Herwegh, M. and Berger, A.: Deformation mechanisms in second-phase affected microstructures and their energy balance, J. Struct. Geol., 26, 1483–1498, https://doi.org/10.1016/j.jsg.2003.10.006, 2004.

Herwegh, M. and Jenni, A.: Granular flow in polymineralic rocks bearing sheet silicates: New evidence from natural examples, Tectonophysics, 332, 309–320, https://doi.org/10.1016/S0040-1951(00)00288-2, 2001.

Herwegh, M., Linckens, J., Ebert, A., Berger, A., and Brodhag, S. H.: The role of second phases for controlling microstructural evolution in polymineralic rocks: A review, J. Struct. Geol., 33, 1728–1750, https://doi.org/10.1016/j.jsg.2011.08.011, 2011.

Herwegh, M., Berger, A., Glotzbach, C., Wangenheim, C., Mock, S., Wehrens, P., Baumberger, R., Egli, D., and Kissling, E.: Late stages of continent-continent collision: Timing, kinematic evolution, and exhumation of the Northern rim (Aar Massif) of the Alps, Earth-Sci. Rev., 200, 102959, https://doi.org/10.1016/j.earscirev.2019.102959, 2020.

Hobbs, B. E., Ord, A., Spalla, M. I., Gosso, G., and Zucali, M.: The interaction of deformation and metamorphic reactions, Geol. Soc. Spec. Publ., 332, 189–223, https://doi.org/10.1144/SP332.12, 2010.

Hofmann, B. A., Helfer, M., Diamond, L. W., Villa, I. M., Frei, R., and Eikenberg, J.: Topography-driven hydrothermal breccia mineralization of Pliocene age at Grimsel Pass, Aar massif, Central Swiss Alps, Schweizerische Mineral. Petrogr. Mitt., 84, 271–302, 2004.

Horwitz, E. P., Dietz, M. L., and Chiarizia, R.: The application of novel extraction chromatographic materials to the characterization of radioactive waste solutions, J. Radioanal. Nucl. Ch., 161, 575–583, https://doi.org/10.1007/bf02040504, 1992.

Humphreys, F. J. and Ardakani, M. G.: Grain boundary migration and zener pinning in particle-containing copper crystals, Acta Mater., 44, 2717–2727, https://doi.org/10.1016/1359-6454(95)00421-1, 1996.

Janots, E., Berger, A., Gnos, E., Whitehouse, M., Lewin, E., and Pettke, T.: Constraints on fluid evolution during metamorphism from U-Th-Pb systematics in Alpine hydrothermal monazite, Chem. Geol., 326/327, 61–71, https://doi.org/10.1016/j.chemgeo.2012.07.014, 2012.

Jessell, M. W.: Grain-boundary migration microstructures in a naturally deformed quartzite, J. Struct. Geol., 9, 1007–1014, https://doi.org/10.1016/0191-8141(87)90008-3, 1987.

Karato, S.-I.: Deformation of Earth Materials: An Introduction to the Rheology of Solid Earth, Cambridge University Press, https://doi.org/10.1007/s00024-009-0536-8, 2009.

Konrad-Schmolke, M., Halama, R., Wirth, R., Thomen, A., Klitscher, N., Morales, L., Schreiber, A., and Wilke, F. D. H.: Mineral dissolution and reprecipitation mediated by an amorphous phase, Nat. Commun., 9, 1637, https://doi.org/10.1038/s41467-018-03944-z, 2018.

Kruse, R. and Stünitz, H.: Deformation mechanisms and phase distribution in mafic high-temperature mylonites from the Jotun Nappe, southern Norway, Tectonophysics, 303, 223–249, https://doi.org/10.1016/S0040-1951(98)00255-8, 1999.

Lanari, P. and Duesterhoeft, E.: Modeling Metamorphic Rocks Using Equilibrium Thermodynamics and Internally Consistent Databases: Past Achievements, Problems and Perspectives, J. Petrol., 60, 19–56, https://doi.org/10.1093/petrology/egy105, 2019.

Lanari, P., Vidal, O., De Andrade, V., Dubacq, B., Lewin, E., Grosch, E. G., and Schwartz, S.: XMapTools: A MATLAB©-based program for electron microprobe X-ray image processing and geothermobarometry, Comput. Geosci., 62, 227–240, https://doi.org/10.1016/j.cageo.2013.08.010, 2014.

Lanari, P., Vho, A., Bovay, T., Airaghi, L., and Centrella, S.: Quantitative compositional mapping of mineral phases by electron probe micro-analyser, Geol. Soc. Spec. Publ., 478, 39–63, https://doi.org/10.1144/SP478.4, 2019.

Law, R. D.: Deformation thermometry based on quartz c-axis fabrics and recrystallization microstructures: A review, J. Struct. Geol., 66, 129–161, https://doi.org/10.1016/j.jsg.2014.05.023, 2014.

Masuda, T., Shibutani, T., Kuriyama, M., and Igarashi, T.: Development of microboudinage: an estimate of changing differential stress with increasing strain, Tectonophysics, 178, 379–387, https://doi.org/10.1016/0040-1951(90)90160-A, 1990.

Masuda, T., Shibutani, T., and Yamaguchi, H.: Comparative rheological behaviour of albite and quartz in siliceous schists revealed by the microboudinage of piedmontite, J. Struct. Geol., 17, 1523–1533, https://doi.org/10.1016/0191-8141(95)00060-Q, 1995.

McDonough, W. F. and Sun, S. S.: The composition of the Earth, Chem. Geol., 120, 223–253, https://doi.org/10.1016/0009-2541(94)00140-4, 1995.

Menegon, L., Fusseis, F., Stünitz, H., and Xiao, X.: Creep cavitation bands control porosity and fluid flow in lower crustal shear zones, Geology, 43, 227–230, https://doi.org/10.1130/G36307.1, 2015.

Morad, S., El-Ghali, M. A. K., Caja, M. A., Sirat, M., Al-Ramadan, K., and Manurberg, H.: Hydrothermal alteration of plagioclase in granitic rocks from Proterozoic basement of SE Sweden, Geol. J., 45, 105–116, https://doi.org/10.1002/gj.1178, 2010.

Mullis, J., Dubessy, J., Poty, B., and O'Neil, J.: Fluid regimes during late stages of a continental collision: Physical, chemical, and stable isotope measurements of fluid inclusions in fissure quartz from a geotraverse through the Central Alps, Switzerland, Geochim. Cosmochim. Ac., 58, 2239–2267, https://doi.org/10.1016/0016-7037(94)90008-6, 1994.

Nègre, L., Stünitz, H., Raimbourg, H., Lee, A., Précigout, J., Pongrac, P., and Jeřábek, P.: Effect of pressure on the deformation of quartz aggregates in the presence of H_2O, J. Struct. Geol., 148, 104351, https://doi.org/10.1016/j.jsg.2021.104351, 2021.

Olgaard, D. L.: The role of second phase in localizing deformation, Geol. Soc. Spec. Publ. 54, 175–181, https://doi.org/10.1144/GSL.SP.1990.054.01.17, 1990.

Oliver, N. H. S. and Bons, P. D.: Mechanisms of fluid flow and fluid-rock interaction in fossil metamorphic hydrothermal systems inferred from vein-wall rock patterns, geometry and microstructure, Geofluids, 1, 137–162, https://doi.org/10.1046/j.1468-8123.2001.00013.x, 2001.

Passchier, C. W. and Trouw, R. A.: Microtectonics, Springer Science & Business Media, ISBN: 978-3-540-29359-0, 2005.

Paterson, M. S.: A theory for granular flow accommodated by material transfer via an intergranular fluid, Tectonophysics, 245, 135–151, https://doi.org/10.1016/0040-1951(94)00231-W, 1995.

Pearce, M. A., Timms, N. E., Hough, R. M., and Cleverley, J. S.: Reaction mechanism for the replacement of calcite by dolomite and siderite: Implications for geochemistry, microstructure and porosity evolution during hydrothermal mineralisation, Contrib. Mineral. Petrol., 166, 995–1009, https://doi.org/10.1007/s00410-013-0905-2, 2013.

Pettke, T., Oberli, F., Audétat, A., Guillong, M., Simon, A. C., Hanley, J. J., and Klemm, L. M.: Recent developments in element concentration and isotope ratio analysis of individual fluid inclusions by laser ablation single and multiple collector ICP-MS, Ore Geol. Rev., 44, 10–38, https://doi.org/10.1016/j.oregeorev.2011.11.001, 2012.

Peverelli, V., Ewing, T., Rubatto, D., Wille, M., Berger, A., Villa, I. M., Lanari, P., Pettke, T., and Herwegh, M.: U-Pb geochronology of epidote by laser ablation inductively coupled plasma mass spectrometry (LA-ICP-MS) as a tool for dating hydrothermal-vein formation, Geochronology, 3, 123–147, https://doi.org/10.5194/gchron-3-123-2021, 2021.

Peverelli, V., Berger, A., Mulch, A., Pettke, T., Piccoli, F., and Herwegh, M.: Epidote U–Pb geochronology and H isotope geochemistry trace pre-orogenic hydration of mid-crustal granitoids, Geology, 50, 1073–1077, https://doi.org/10.1130/G50028.1, 2022.

Pongrac, P., Jeřábek, P., Stünitz, H., Raimbourg, H., Heilbronner, R., Racek, M., and Nègre, L.: Mechanical properties and recrystallization of quartz in presence of H_2O: Combination of cracking, subgrain rotation and dissolution-precipitation processes, J. Struct. Geol., 160, 104630, https://doi.org/10.1016/j.jsg.2022.104630, 2022.

Putnis, A.: Mineral replacement reactions, Rev. Mineral. Geochem., 70, 87–124, https://doi.org/10.2138/rmg.2009.70.3, 2009.

Putnis, A. and Austrheim, H.: Fluid-induced processes: Metasomatism and metamorphism, Geofluids, 10, 254–269, https://doi.org/10.1111/j.1468-8123.2010.00285.x, 2010.

Putnis, A. and John, T.: Replacement processes in the earth's crust, Elements, 6, 159–164, https://doi.org/10.2113/gselements.6.3.159, 2010.

Ramseyer, K., Baumann, J., Matter, A., and Mullis, J.: Cathodoluminescence Colours of α-Quartz, Mineral. Mag., 52, 669–677, https://doi.org/10.1180/minmag.1988.052.368.11, 1988.

Rehkämper, M. and Mezger, K.: Investigation of matrix effects for Pb isotope ratio measurements by multiple collector ICP-MS: Verification and application of optimized analytical protocols, J. Anal. At. Spectrom., 15, 1451–1460, https://doi.org/10.1039/b005262k, 2000.

Ricchi, E., Bergemann, C. A., Gnos, E., Berger, A., Rubatto, D., and Whitehouse, M. J.: Constraining deformation phases in the Aar Massif and the Gotthard Nappe (Switzerland) using Th-Pb crystallization ages of fissure monazite-(Ce), Lithos, 342/343, 223–238, https://doi.org/10.1016/j.lithos.2019.04.014, 2019.

Rolland, Y., Cox, S. F., and Corsini, M.: Constraining deformation stages in brittle-ductile shear zones from combined field mapping and ^{40}Ar / ^{39}Ar dating: The structural evolution of the Grimsel Pass area (Aar Massif, Swiss Alps), J. Struct. Geol., 31, 1377–1394, https://doi.org/10.1016/j.jsg.2009.08.003, 2009.

Rossi, M. and Rolland, Y.: Stable isotope and Ar / Ar evidence of prolonged multiscale fluid flow during exhumation of orogenic crust: Example from the mont blanc and Aar Massifs (NW Alps), Tectonics, 33, 1681–1709, https://doi.org/10.1002/2013TC003438, 2014.

Ruiz, M., Schaltegger, U., Gaynor, S. P., Chiaradia, M., Abrecht, J., Gisler, C., Giovanoli, F., and Wiederkehr, M.: Reassessing the intrusive tempo and magma genesis of the late Variscan Aar batholith: U-Pb geochronology, trace element and initial Hf isotope composition of zircon, Swiss J. Geosci., 115, 1–24, https://doi.org/10.1186/s00015-022-00420-1, 2022.

Schaltegger, U. and Krähenbühl, U.: Heavy rare-earth element enrichment in granites of the Aar Massif (Central Alps, Switzerland), Chem. Geol., 89, 49–63, https://doi.org/10.1016/0009-2541(90)90059-G, 1990.

Schaltegger, U. and Corfu, F.: The age and source of late Hercynian magmatism in the central Alps: evidence from precise U-Pb ages and initial Hf isotopes, Contrib. Mineral. Petrol., 111, 329–344, https://doi.org/10.1007/BF00311195, 1992.

Schmidt, M. W. and Poli, S.: Magmatic epidote, Rev. Mineral. Geochem., 56, 399–430, https://doi.org/10.2138/gsrmg.56.1.399, 2004.

Schneeberger, R., Kober, F., Spillmann, T., Blechschmidt, I., Lanyon, G. W., and Mäder, U. K.: Grimsel Test Site: revisiting the site-specific geoscientific knowledge (NTB–19-01), Switzerland, 2019.

Seydoux-Guillaume, A., Montel, J., Bingen, B., Bosse, V., De Parseval, P., Paquette, J., Janots, E., and Wirth, R.: Low-temperature alteration of monazite: Fluid mediated coupled dissolution – precipitation, irradiation damage, and disturbance of the U–Pb and Th–Pb chronometers, Chem. Geol., 330/331, 140–158, https://doi.org/10.1016/j.chemgeo.2012.07.031, 2012.

Stipp, M., Stünitz, H., Heilbronner, R., and Schmid, S. M.: Dynamic recrystallization of quartz: correlation between natural and experimental conditions, Geol. Soc. Lond. Sp. Publ., 200, 171–190, https://doi.org/10.1144/GSL.SP.2001.200.01.11, 2002.

Stünitz, H. and Fitz Gerald, J. D. F.: Deformation of granitoids at low metamorphic grade, II: Granular flow in albite-rich mylonites, Tectonophysics, 221, 299–324, https://doi.org/10.1016/0040-1951(93)90164-F, 1993.

Tartèse, R., Ruffet, G., Poujol, M., Boulvais, P., and Ireland, T. R.: Simultaneous resetting of the muscovite K-Ar and monazite U-Pb geochronometers: A story of fluids, Terra Nova, 23, 390–398, https://doi.org/10.1111/j.1365-3121.2011.01024.x, 2011.

Tera, F. and Wasserburg, G. J.: U-Th-Pb systematics in three Apollo 14 basalts and the problem of initial Pb in lunar rocks, Earth Planet. Sc. Lett., 14, 281–304, https://doi.org/https://doi.org/10.1016/0012-821X(72)90128-8, 1972.

Trincal, V., Lanari, P., Buatier, M., Lacroix, B., Charpentier, D., Labaume, P., and Muñoz, M.: Temperature micro-mapping in oscillatory-zoned chlorite: Application to study of a green-schist facies fault zone in the Pyrenean Axial Zone (Spain), Am. Mineral., 100, 2468–2483, https://doi.org/10.2138/am-2015-5217, 2015.

Tullis, J.: Deformation of granitic rocks: Experimental studies and natural examples, Rev. Mineral. Geochem., 51, 51–95, https://doi.org/10.2138/gsrmg.51.1.51, 2002.

Villa, I. M. and Hanchar, J. M.: K-feldspar hygrochronology, Geochim. Cosmochim. Ac., 101, 24–33, https://doi.org/10.1016/j.gca.2012.09.047, 2013.

Wehrens, P., Berger, A., Peters, M., Spillmann, T., and Herwegh, M.: Deformation at the frictional-viscous transition: Evidence for cycles of fluid-assisted embrittlement and ductile deformation in the granitoid crust, Tectonophysics, 693, 66–84, https://doi.org/10.1016/j.tecto.2016.10.022, 2016.

Wehrens, P., Baumberger, R., Berger, A., and Herwegh, M.: How is strain localized in a meta-granitoid, mid-crustal basement section? Spatial distribution of deformation in the central Aar massif (Switzerland), J. Struct. Geol., 94, 47–67, https://doi.org/10.1016/j.jsg.2016.11.004, 2017.

Weis, D., Kieffer, B., Maerschalk, C., Barling, J., De Jong, J., Williams, G. A., Hanano, D., Pretorius, W., Mattielli, N., Scoates, J. S., Goolaerts, A., Friedman, R. M., and Mahoney, J. B.: High-precision isotopic characterization of USGS reference materials by TIMS and MC-ICP-MS, Geochem. Geophy. Geosy., 7, Q08006, https://doi.org/10.1029/2006GC001283, 2006.

Williams, M. L., Jercinovic, M. J., Harlov, D. E., Budzyń, B., and Hetherington, C. J.: Resetting monazite ages during fluid-related alteration, Chem. Geol., 283, 218–225, https://doi.org/10.1016/j.chemgeo.2011.01.019, 2011.

Wintsch, R. P. and Yeh, M. W.: Oscillating brittle and viscous behavior through the earthquake cycle in the Red River Shear Zone: Monitoring flips between reaction and textural softening and hardening, Tectonophysics, 587, 46–62, https://doi.org/10.1016/j.tecto.2012.09.019, 2013.